



Slow-drift of a floating wind turbine: An assessment of frequency-domain methods based on model tests



Alexandre N. Simos^{a,*}, Felipe Ruggeri^a, Rafael A. Watai^a, Antonio Souto-Iglesias^b, Carlos Lopez-Pavon^c

^a Dept. of Naval Arch. & Ocean Eng. Escola Politécnica, University of São Paulo, São Paulo, Brazil

^b CEHINAV, DMFPA, ETSIN, Universidad Politécnica de Madrid, Madrid, Spain

^c COREMARINE, Madrid, Spain (formerly in ACCIONA, Spain)

ARTICLE INFO

Article history:

Received 30 July 2016

Received in revised form

21 August 2017

Accepted 16 September 2017

Available online 23 September 2017

Keywords:

Floating offshore wind turbine (FOWT)

Semisubmersible

Mooring design

Slow-drift forces

Model tests

QTFs computation

White-noise approximation

ABSTRACT

The second-order hydrodynamics of a semisubmersible offshore wind turbine is investigated in this paper by analyzing and proposing a set of different options for estimating the slow-drift motions during its design. A case study consisting of a three-floater semisubmersible designed to support a 1.5Mw turbine is considered. An experimental campaign focused on characterizing second-order surge response was carried out and its most salient results are documented in the paper. The campaign was conducted in two different facilities and comprised decay tests, regular, bichromatic and irregular waves. Wind has not been considered in this phase of the research. Numerical modeling with frequency domain solver WAMIT has been carried out. Due to location depth and mooring length restrictions, the natural periods of horizontal excursions are smaller than those of well studied DeepCwind platform. This may change the importance of the different second-order components, something investigated in present research by comparing simplified and full Quadratic Transfer Functions (QTF) computations. Results obtained with experiments and simulations are compared, focusing on the mean and slow-drift motions and forces. It is shown that the Newman approximation underestimates the second-order response in some cases while the white noise model retains the main physics involved, a novel result which may change the paradigm for mooring design of these artifacts in the near future.

© 2017 Elsevier Ltd. All rights reserved.

1. Introduction

The interest of the electric power generation sector in floating offshore wind turbines (FOWTs) is growing up. This interest is exemplified in the recent successful launch and test of full scale prototypes: Hywind in Norway [1], WindFloat in Portugal [2], Mitsui in Japan [3] and VolturnUS, the 1:8 large scale unit of university of Maine [4,5]. The reason for this interest is that 61% of the US coastal areas, nearly all of Japan's, and various European locations such as off the coast of Norway and Mediterranean, require floating foundation technology due to large water depths.

Among the FOWTs platforms, three concepts have emerged as the most attractive: TLP, spar and semisubmersible. In particular the semisubmersible concept has received attention in the recent literature (see e.g. Refs. [2,6]) due to several claimed advantages [7],

namely: these types of platforms can be fully assembled onshore and towed ready-to-use to their final destinations; the available mooring systems are well-known and cost competitive; if properly designed, downtime in operational sea states, due to excessive platform motion, is low.

One common feature of offshore floating platforms is that, in order to avoid resonance in the wave energy range, the design natural periods for some of the motions are quite large (or low in the case of the TLP concept). In addition, although not as large as typically observed for floating units in deep waters, FOWTs with conventional catenary mooring systems still present large natural periods of horizontal excursions. This brings the need to look at wave second-order excitations.

Goupee et al. [8,9] conducted experiments with representative designs of the three prevalent FOWTs concepts within DeepCwind R&D U.S. project. They excited the floaters with irregular seas and found that low frequency surge motions can be quite energetic for the semisubmersible concept. Some of these authors also

* Corresponding author.

E-mail address: alesimos@usp.br (A.N. Simos).

documented different aspects of the experimental setup [10–12] without however paying specific attention to the challenges of directly characterizing the second-order response of the floaters by experimentally evaluating their QTFs.

Roald et al. [13] studied the second-order forces of a spar (OC3-Hywind) platform and a TLP (UMaine), trying to assess their relevance when compared to aerodynamic ones. Coulling et al. [14] focused, however, on the semisubmersible concept using Goupee et al.'s [8] experimental data to validate the implementation of second-order wave forces in FAST time domain solver. They used Newman approximation to compute the QTF [15], thus implying only mean-drift terms, which can be obtained from first-order potential, were accounted for. They largely improved the estimation of the surge response spectrum when compared to considering just first-order forces. However, they needed to modify/tune damping obtained from decay tests in order to accurately reproduce such motion spectrum. In addition, their platform had a quite large surge natural period (~ 100 seconds), fundamental for the accuracy of Newman's approximation, which may not be representative of the behavior of other floaters, mainly those working in shallower waters (it must be borne in mind that the water depths of as important floating devices testing sites as BIMEP in Spain, the recently approved Mistral in France, and WindFloat location, range between 42 and 90 m). Goupee et al. [8] looked as well at the mooring tensions, whose predictions showed reduced accuracy compared to that of the motions, something that they attributed to a poor representation of the mooring dynamics.

Gueydon et al. [16] compared computations of second-order forces using WAMIT and DIFRAC codes. While WAMIT is able to compute all second-order force components, DIFRAC is able to compute only those that depend on first-order potential. They conducted time domain simulations using FAST and aNySYM, taking frequency domain forces and added masses from WAMIT and DIFRAC respectively. They used the DeepCwind semisubmersible floater geometry but did not compare with experimental data. Subtle issues regarding the damping modeling are documented, and only minor differences between the two solvers simulations are found. The lead author of such reference had previously considered as well some second-order effects with DIFRAC-aNySYM [17,18] but the formulation was not clearly explained and validation was jointly conducted while considering wind effects, something that makes it difficult to isolate the accuracy of the modeling of second-order wave forces effects.

Jiawen Li et al. [19] proposed a novel hybrid spar-semisubmersible concept for floating offshore wind turbines. In order to analyze it, they implemented a coupled time domain solver using FAST, with first and second-order wave forces (full QTF) obtained in frequency domain with WADAM. In order to validate their approach, they simulated one irregular motion case of the OC4 platform, also studied by Coulling et al. [14]. Jiawen Li et al. [19] results for that case, in terms of surge PSD, were overall similar to those of Coulling et al.'s [14] and they claimed a better representation of the secondary coupled pitch resonance peak. However, the scope of their analysis was quite limited, natural period was high for this case, which makes Newman approximation to be likely in agreement with the full QTF, and discussion on added damping values was not included.

Bayati et al. [20] analyzed, numerically, the second-order hydrodynamics of again the DeepCwind semi floater. They linearized the topside response computed with FAST in order to incorporate its effect into frequency domain computations carried out with WAMIT. They used the full QTF to characterize the second-order response, without explicitly discussing how different compared to the Newman approximation the outcome was. They noted that the predicted second-order effects seemed reminiscent of those

found in Ref. [8] irregular motion tests. Bayati et al. [20] also showed that low frequency response due to second-order hydrodynamics dominates over the combined wind and first-order wave effects for large wave heights. This fact provides extra meaning to present analysis, where only the platform hydrodynamics is considered.

Lopez-Pavon et al. [21] (our previous work, with the same semisubmersible floater studied in the present research) conducted tests with the model fixed in bichromatic waves, in order to measure second-order loads directly and assess the accuracy of different numerical approximations to model such effects. The scope of the campaign was somewhat limited, but sufficient results were gathered to document, for example, that Newman's approximation could be not accurate enough for the modeling of that particular floater. This was mainly due to the relatively low resonance periods imposed by the design mooring system, leading to increased errors in this approximation.

Bayati et al. [22] extended their referred 2014 work [20], with water depth of 200 m, to lower water depths down to 30 m. Apart from the second-order hydrodynamics, they also accounted for the setdown effect in the time history of the incoming waves. Due to its low resonance frequency, they found first-order heave motion to be the most affected by reducing the water depth, since corresponding waves were long enough to be significantly affected by the presence of the seabed. They found no significant influence of reduced water depth on second-order surge nor pitch motions when changing it from 200 m to around 60 m. Only when a shallow depth of 30 m was reached, a substantial increase of the mean and oscillating components of surge and pitch motions was observed. In this work, they kept the same surge natural period (~ 120 s) regardless of the depth choice. This, however, may be unrealistic since, for catenary moorings, lower depth is usually associated to a lower natural period.

All these analysis ultimately are carried out to assess the impact of second-order hydrodynamics on the mooring design, and the short literature review presented above reveals the absence of a more systematic experimental and numerical analysis planned for investigating, specifically, the slow drift components.

Designing the mooring of a floating offshore wind turbine is a complex matter due to the fact that wind, wave and current loads and coupled structural dynamics have to be accounted for Refs. [23–27]. Accurately assessing second-order slow-drift forces is necessary for an optimized design of the mooring system [21,28]. In addition, it is known that the cost of such mooring system is a major component of the initial investment [29]. Therefore, cost reductions due to an optimized design can be crucial in order to attain a competitive alternative.

Motivated by the considerations above, the focus of this paper is on measurement, estimation and verification of the second-order wave induced forces and motions on a semi-submersible floater operating in lower depth than the one of OC4-DeepCwind and with lower natural periods of excursion. Moreover, the work aims at verifying the main preconditions for defining a proper second-order diffraction model, given that different approximations are available for obtaining the QTFs (and acknowledging that a clever choice can significantly reduce the amount of work required for both building and solving the numerical model).

With these goals in mind, first the paper provides a quick theoretical background on the mathematical description of the slow-drift forces, with a reminder on the main approximations that are available for computing them. Next, the model-scale case-study is presented, with a general overview of the floater and mooring models and details on the experimental setup. This is followed by a description of the numerical model, in which the meshing procedures and convergence are discussed, together with an

explanation on how the different approximations tested for computing the QTFs are dealt with. The subsequent sections comprise the analysis and comparison of the results obtained from experiments and numerical simulations, including mean-drift forces, slow motions recorded in bichromatic wave tests and the model drifts observed in irregular wave conditions. Finally, conclusions and future work topics are listed.

To the authors' knowledge, no similar comprehensive and systematic analysis on the slow-drifts of a floating wind turbine can be found in literature. The authors have tried to report all the important steps involved in the numerical analysis vis a vis the corresponding results obtained in the experiments. This procedure has allowed a thorough discussion on the many aspects involved, such as in the generation of the numerical meshes, the validity of the various options available for computing the QTF, the attention that must be paid to the evaluation of the viscous damping, etc. All these topics frequently raise doubts during the design of mooring systems and, therefore, such discussions have been deemed necessary.

2. Theoretical background

The solution of the nonlinear wave diffraction problem up to second-order gained attention in the late 1970's and a rich overview of the theoretical developments is given, for example, by Refs. [30,31]. For the sake of discussing the main aspects regarding the computation of the hydrodynamic loads, the formulation as proposed by Pinkster [32] will be followed next. In his description, the second-order low-frequency forces are written (in a moving non-rotating frame of reference with origin in the body's center of gravity) as the summation of five different components:

$$\begin{aligned} \vec{F}^{(2)}(t) = & \iint_{\bar{S}_B} \left(-\rho \frac{\partial \phi^{(2)}}{\partial t} \right) \vec{n}^{(0)} dS + \phi_{WL} \frac{1}{2} \rho g \left(\zeta_r^{(1)} \right)^2 \vec{n}^{(0)} dl \\ & + \iint_{\bar{S}_B} \left(-\frac{1}{2} \rho \nabla \phi^{(1)} \cdot \nabla \phi^{(1)} \right) \vec{n}^{(0)} dS \\ & + \iint_{\bar{S}_B} \left(-\rho \vec{X}^{(1)} \cdot \nabla \frac{\partial \phi^{(1)}}{\partial t} \right) \vec{n}^{(0)} dS - m [R^{(1)}] \{ \ddot{\vec{X}}^{(1)} \} \end{aligned} \quad (1)$$

In the equation above, $\phi^{(1)}$ and $\phi^{(2)}$ represent the first and second-order velocity potentials, respectively. $\vec{X}^{(1)}$ and $\ddot{\vec{X}}^{(1)}$ denote the first-order (wave-frequency) body translations and accelerations, while $\zeta_r^{(1)}$ indicates the wave elevation relative to the body axes along the body's waterline. The vector $\vec{n}^{(0)}$ is the mean value in time of the inward body normal, thus representing the normal vector of the mean body surface \bar{S}_B , while $[R^{(1)}]$ denotes a linearized rotation matrix considering the body's angular motions. The details regarding the derivation of this formulation, as well as those concerning the adopted coordinate systems are not reproduced here, for the main intention is only to discuss some practical aspects involved in the numerical computation of each force term.

The first force component in Eq. (1) brings the contribution of the second-order potential. Without any further simplification of the seakeeping problem, this is the most difficult component to compute, the one that ultimately requires a more complex numerical model for tackling the solution of the second-order BVP. In fact, following the classical perturbation method on which this theoretical model is based, the solution of the second-order BVP is forced by the solution of the first-order one, which must be obtained beforehand. An important consequence is that the second-order free-surface boundary condition is an inhomogeneous PDE

that is not automatically satisfied by the Green Function used by most radiation-diffraction codes based on Boundary-Element Methods for the solution of the first-order problem (WAMIT® included). As a result, for the numerical solution of the second-order problem, not only the body surface but also the entire mean (undisturbed) free-surface must be taken into account as part of the problem boundary and discretized. In general, the free-surface mesh leads to a significant increase in the dimension of the mathematical problem and, in practice, it renders the numerical convergence of the solution much more difficult to guarantee. Furthermore, the solution of the second-order problem also results much more time consuming if compared to the linear solution. It is important to recall that, since this force component has zero mean, it does not contribute for the computation of the mean-drift but only for the difference and sum-frequency second-order components.

All the four other components in Eq. (1) represent quadratic contributions of the first-order solution and may be computed based exclusively on the solution of the first-order problem. However, although they are indeed much quicker to evaluate if compared to the contribution of the second-order potential, their computation also is not free of risks. One should remind, for example, that the numerical computation of the flow velocity (gradient of the velocity potential) on the body surface in a low-order discretization scheme¹ requires a much more refined mesh in order to guarantee numerical convergence. In addition, as the forces depend on the first-order motions (displacements, velocities and accelerations), appropriate damping considerations must be made in order to avoid spurious amplifications and over prediction of quantities near the resonant frequencies. It can also be shown (see e.g. Ref. [32]), that the forces that are represented in Eq. (1) as a function of time may alternatively be written in the frequency domain by considering pairs of sinusoidal wave components with frequencies $(\omega_i; \omega_j)$, as indicated in Eq. (2), below, for the force in the d.o.f. denoted by α :

$$F_{2,\alpha}(t) = \text{Re} \sum_i \sum_j A_i A_j T_\alpha(\omega_i; \omega_j) \exp\{ -i[\omega_i - \omega_j]t + \varepsilon_i - \varepsilon_j \} \quad (2)$$

here A_i, A_j represent the wave amplitudes and $\varepsilon_i, \varepsilon_j$ the corresponding phases. The function $T_\alpha(\omega_i; \omega_j)$ corresponds then to the amplitude of the second-order force per unitary wave amplitudes and is known as the quadratic transfer function (QTF).

By the definition of the QTF in Eq. (2), one may readily see that for pairs with the same frequency $(\omega_i = \omega_j)$ its value corresponds to the mean-drift force, i.e.:

$$T_\alpha(\omega; \omega) = D_\alpha(\omega). \quad (3)$$

Due to the inherent numerical difficulties faced in the computation of the QTFs, some approximations for the evaluation of the slow-drift forces have been proposed in the literature, mainly aiming at avoiding the problems associated with the calculation of the second-order potential $\phi^{(2)}$. Among these approximations, the one that is most widely used is the so-called Newman's approximation [15], which makes use of some symmetry properties of the QTF matrix to derive an approximation based exclusively on the mean drift forces. This approximation is valid for deep water problems under certain conditions that will be discussed next. One of the forms in which Newman's approximation is often used is

¹ The so-called low-order methods represent the body geometry by means of flat panels and the velocity potential is considered constant over each panel surface.

given in Eq. (4), where $\delta\omega = \omega_i - \omega_j$,

$$T_\alpha(\omega; \omega + \delta\omega) \cong D_\alpha(\omega + \delta\omega/2). \quad (4)$$

The main advantage in using Newman's approximation comes from the fact that, as explained above, the mean-drift forces can be computed exclusively from the results of the first-order solution. However, one should notice that the validity of the approximation is based on the supposition that the frequency difference ($\delta\omega$) is small, because the error involved in adopting it is of the order $\mathcal{O}(\delta\omega^2)$ (see e.g. Ref. [33]). For large offshore systems in deep waters (such as oil production semis and FPSOs), which normally have natural periods of drift well above 100s, Newman's approximation is acknowledged as a useful method for estimating the slow-drift forces. However, as the resonance periods decrease, the errors involved in its application may result unacceptable for design purposes.²

For the FOWT considered in this study, with natural periods of surge and sway around 75 s, the accuracy associated to the application of Newman's approximation is uncertain. Ahead in this paper, the results obtained with the use of this approximation will be assessed in the light of the experimental results and by comparing them to the those obtained from full QTF computations.

Another approximation, yet one of a different kind, may be envisaged for reducing the computational burden for evaluating the QTF matrix: the use of the so-called white-noise approach. In fact, this is not an approximation on the computation of the second-order force (as is the case with Newman's approximation) but rather a proposal through which the relevant band of frequencies of the QTF matrix is identified. It is inspired in the classical methodology proposed by Crandall and Mark [35] for the analysis of mechanical systems with narrow-banded response. The idea is quite simple: since the resonant drift motions are usually weakly damped, the motion spectrum is narrow-banded, meaning that only the QTF values in a narrow band around the natural frequency effectively contribute for the slow-drift motions. The approximation made is, then, to suppose that the second-order force spectrum may be deemed constant (thus a 'white-noise' approach) inside this band. The method may be implemented in more than one way and the one adopted here follows the work of Matos et al. [34], who successfully applied the white-noise approach for the study of a deep-draft semi-submersible. For this, it is assumed that the motion under analysis may be decoupled from the other rigid body motions. It will be shown ahead that this is, indeed, a reasonable assumption for the slow-drift motions recorded along the model tests. Although there are, for sure, dynamical couplings involved (especially the surge-pitch one), the effects on the surge motions are generally small. Therefore, considering only the α motion, the second-order response spectrum may be written as:

$$S_\alpha^{(2)}(\omega) \cong |H_\alpha(\omega)|^2 S_{F,\alpha}^{(2)}(\omega), \quad (5)$$

where $S_\alpha^{(2)}$ denotes the second-order force spectrum and $H_\alpha(\omega)$ represents a transfer function for an unitary force. The latter can be easily computed as:

$$H_\alpha(\omega) = \frac{1}{-\omega^2(M_{\alpha\alpha} + A_{\alpha\alpha}) + i\omega(B_{\alpha\alpha} + B'_{\alpha\alpha}) + (C_{\alpha\alpha} + C'_{\alpha\alpha})}. \quad (6)$$

In the equation above, A , B and C respectively represent the

added mass, potential damping and hydrostatic stiffness for the α motion, while B' indicates an external linearized (viscous) damping and C' considers an external linearized (mooring) stiffness. The second-order force spectrum in the difference-frequencies is computed from the QTFs in the following way (see for instance Ref. [32]):

$$S_{F,\alpha}^{(2)}(\delta\omega) = 8 \int_0^\infty S(\omega)S(\omega + \delta\omega)|T_\alpha(\omega; \omega + \delta\omega)|^2 d\omega. \quad (7)$$

The white-noise approximation assumes that, for practical purposes, the force spectrum in Eq. (7) may be considered constant and that its magnitude is the one computed when $\delta\omega = \omega_{n,\alpha}$. Therefore, the second-order response spectrum for the low-frequency motions can be computed simply as:

$$S_\alpha^{(2)}(\delta\omega) \cong |H_\alpha(\delta\omega)|^2 S_{F,\alpha}^{(2)}(\omega_{n,\alpha}). \quad (8)$$

The advantage in using Eq. (8) is that the QTF matrix does not need to be computed for the many pairs ($\omega_i = \omega_j$), but only for the ones in the diagonal corresponding to $\omega_i - \omega_j = \omega_{n,\alpha}$. Usually this allows a significant reduction of computation effort and also avoids the risk of numerical errors that may occur when computing QTF coefficients for frequency differences that should not effectively contribute for the slow motions. Furthermore, it should be emphasized that the use of the white-noise approach does not involve an approximation of the QTF itself. It can, therefore, be used in addition to other approximations (for example disregarding the influence of the second-order potential or computing the QTFs according to Newman's approximation) if they are appropriate for the particular system that is being analyzed. The advantages associated to the use of the white-noise approach will be discussed in more details in Section 4, when the slow-drift motions of the floater model in irregular waves are investigated.

The study regarding the slow motions in irregular waves is usually performed following two different approaches:

1. Computing the "complete" second-order motion RAOs, in which all hydrodynamic/external couplings are considered, with the RAOs computed numerically using a potential flow solver, for instance, WAMIT 2nd order module;
2. From the second-order force operators, which are also evaluated from a potential flow solver. In this case, however, the second-order motion RAOs are evaluated assuming that the motions are uncoupled. In fact, this is a fair approximation for the horizontal motions of the floater in the present study, something that can be apprehended from the RAOs in Fig. 1. One may notice that the surge/pitch coupling change the pitch RAO appreciably, especially around the surge natural period ($\sim 75s$). On the other hand, the additional pitch stiffness introduced by the mooring lines does not seem to impose any significant change on the surge RAO. The errors introduced when neglecting the dynamic couplings for modeling the slow-drifts according to the white-noise approach should, therefore, be small.

3. Case study

3.1. Prototype

3.1.1. Floater

The floater has been the main outcome of HiPRWind EU project, on hold since the Spanish government 2012 cut off the feed-in tariff for renewable energy. The structure of the floater consists of three

² One may refer to the discussion provided by Ref. [34] on this subject when dealing with the similar problem of resonant roll and pitch motions of a semi-submersible platform.

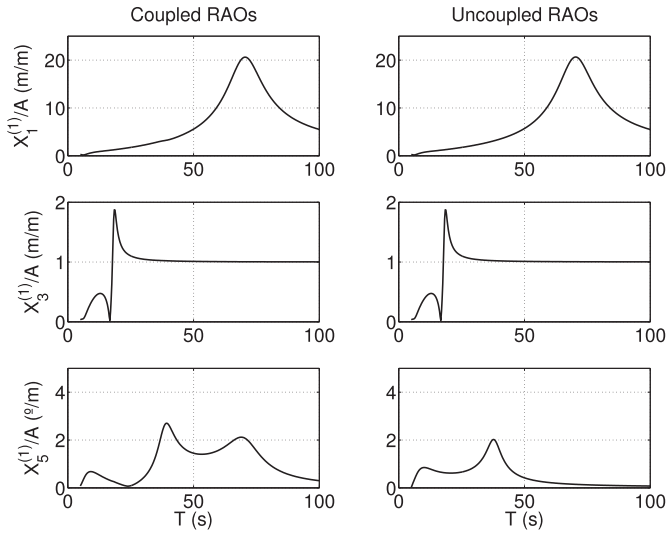


Fig. 1. Comparison of the first-order response amplitude operators considering coupled and decoupled motions in surge (top), heave (center) and pitch (bottom).

vertical columns linked by several braces. A circular heave plate is added to the bottom of each column, as a mean to increase the natural heave period and, as a consequence, to prevent large resonant motions in both operational and survival sea states.

The main dimensions of the platform are given in Table 1 and a schematic view of the floater geometry is presented in Fig. 2. The depth-radius ratio of the heave plate can be considered large (~ 1.5). To put this figure in perspective, it must be noted that, for example, Wadhwa and Thiagarajan [36]; in their specific work regarding free surface influence in hydrodynamic coefficients, considered only depth-radius ratios lower than 0.5. With the present ratio (1.55), it is expected that viscous damping will be dominant with respect to radiation damping. The heave plates are equipped with some structural reinforcements including a vertical flap edge. The influence of these elements in the damping characteristics of the platform has been subject of a separate piece of research [37].

In order to have a proper perspective of the present case study, its main dimensions are compared with DeepCwind and WindFloat projects in Table 2. Operation depth is different across the three units. DeepCwind depth is 200 m compared to 100 m for current research. DeepCwind tests are well documented in the literature, with a surge natural period significantly larger than present one (107s compared to approx. 75s). On the other hand, the model scale

Table 1
Main dimensions of the platform (prototype and model scale).

Characteristic	Symbol	Prototype	Model
Platform draft, disc depth	h	15.5 m	0.775 m
Column center to center	c	35 m	
Columns diameter	D_c	7.0 m	0.35 m
Heave plate (disc) diameter	D_d	20 m	1.0 m
Heave plate (disc) thickness	t_d	~10 mm	5 mm
Platform Displacement (with mooring)	Δ	2446 t	307.5 kg
Platform Displacement (without mooring)	Δ'	2332 t	293.1 kg
Water depth	H'	100 m	5 m
Natural period (surge - horizontal mooring)	T_1^r	75.6 s	16.9 s
Natural period (surge - real mooring)	T_1^r	74.8 s	16.7 s
Natural period (heave - free floating)	T_3	19.2 s	4.3 s
Natural period (pitch - horizontal mooring)	T_5^r	26.2 s	5.9 s
Natural period (pitch - real mooring)	T_5^r	25.4 s	5.7 s
Model scale	λ		19.8



Fig. 2. Semisubmersible platform case study sketch.

Table 2
Comparison of main dimensions between current design, DeepCwind [6] and WindFloat [2].

Symbol	Current	DeepCwind	WindFloat
h	15.5 m	20 m	22.9 m
c	35 m	50 m	46 m
D_c	7.0 m	12 m	10 m
D_d	20 m	24 m	35.8 m
h/r_d	1.53	1.67	1.56
Δ	2446 t	13444 t	7105 t
Δ'	2332 t	14265 t	
H'	90 m	200 m	42 m
P'	1.5 Mw	5 Mw	2 Mw
λ	19.8	50	78
n	3	3	3
T_1^r	74.8 s	107 s	108.6 s
T_3	19.2 s	17.5 s	19.9 s
T_5^r	25.4 s	26.8 s	43.2 s

dimensions of present research specimen are significantly larger than those of the aforementioned reference designs, which is a remarkable fact since it may help in reducing scale effects.

3.1.2. Mooring

The mooring (Fig. 3) is composed of three catenary lines connected at the top of each column. The complete mooring system is highly pretensioned and relative small excursions are allowed to prevent any collisions between mooring chains and heave plates during extreme events. Another limitation for the mooring design is the reduced area for anchor installation, due to the small area of the test zone available for the platform (less than 500 m radius for anchor installation). The chain has been oversized in weight to provide a high catenary effect and to prevent any vertical uplift of

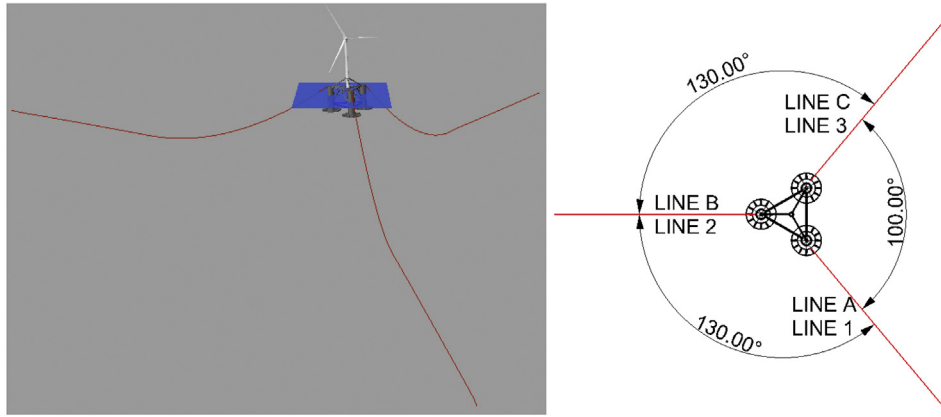


Fig. 3. Mooring configuration.

the drag anchor selected. A relevant aspect to highlight is that the mooring lines configuration is not symmetric, the reason being the directionality of wave and wind spectra.

3.1.3. Environmental conditions

The prototype is to be installed at BIMEP testing site, located 2 km off the coast in northern Spain, with depths ranging between 50 and 90 m. Wind has not been considered in present analysis and therefore, the focus is on wave statistics, for which a significant wave height, H_s , rose is presented in Fig. 4. As can be appreciated in the figure, and due to the proximity to the coast, the sea is extremely directional. A wind rose is also presented; though not so extremely directional as the waves, a similar trend can be appreciated. The combination of both effects is the justification for the non-symmetric mooring presented in Fig. 3.

3.2. Experimental setup

3.2.1. Model

A 1:19.8 scale model of the floater was built and tested in two different wave basin facilities, namely the Hydrodynamics & Ocean Energy Wave Tank at Ecole Centrale de Nantes (ECN) in France and

the Canal de Ensayos Hidrodinamicos de El Pardo (CEHIPAR) in Spain. The model scale was chosen so that the tank depth, which was the same in both facilities, would be representative of the water depth at prototype location, taken as 100 m. In this way, simple catenary chain models could be adopted for keeping the model position, without the need to compensate for any difference in depth. An image of the model, about to be deployed in the ECN tank, is presented in Fig. 5. The characteristics of the model have been included, together with those of the prototype, in Table 1. For the ECN tests, both an emerged horizontal mooring and a model of the real catenary chains mooring were tested (characteristics of both mooring systems in Table 1). In the tests performed at CEHIPAR, only the real mooring model was tested.

3.2.2. Experimental facility and measuring gear

ECN's wave basin is 50 m long, 30 m wide and 5 m deep. In this tank, tests were performed with regular (monochromatic) and bichromatic waves, aiming at verifying the performance of the numerical models in reproducing mean and slow motions for selected pairs of frequencies. All tests in both tanks involved only bow waves. An sketch of the arrangement of the mooring lines in the ECN tank is presented in Fig. 6. The arrangement at CEHIPAR

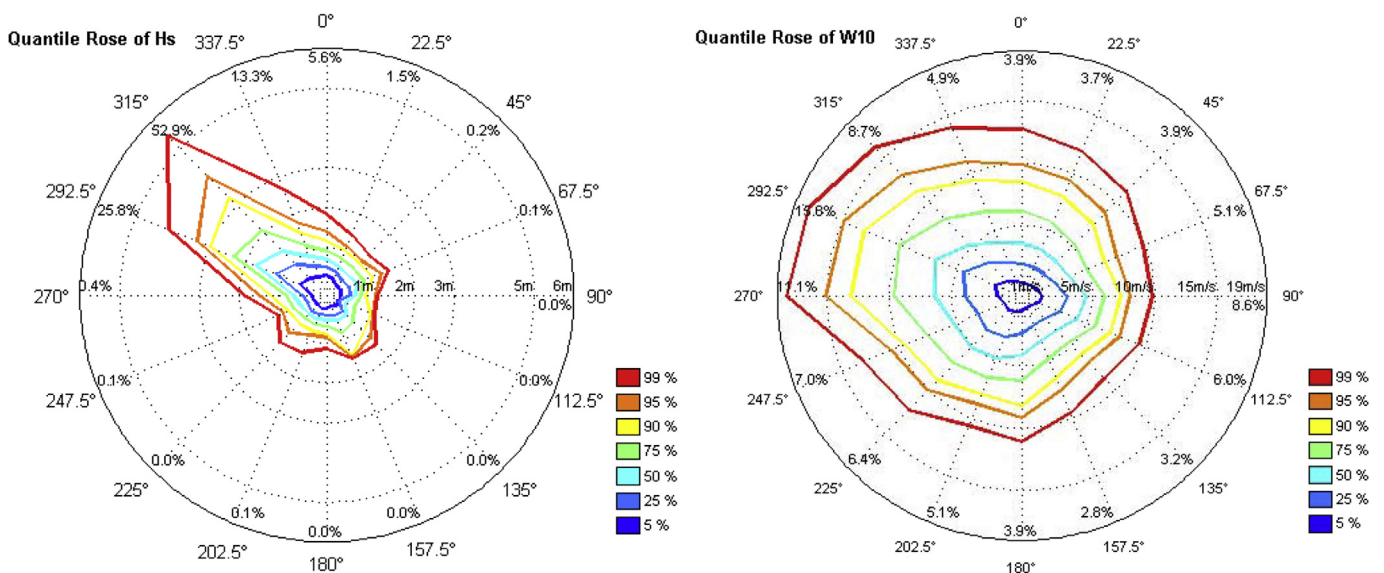


Fig. 4. Significant wave height (left) and wind speed (right) roses for prototype location (BIMEP)-Ref. [38].

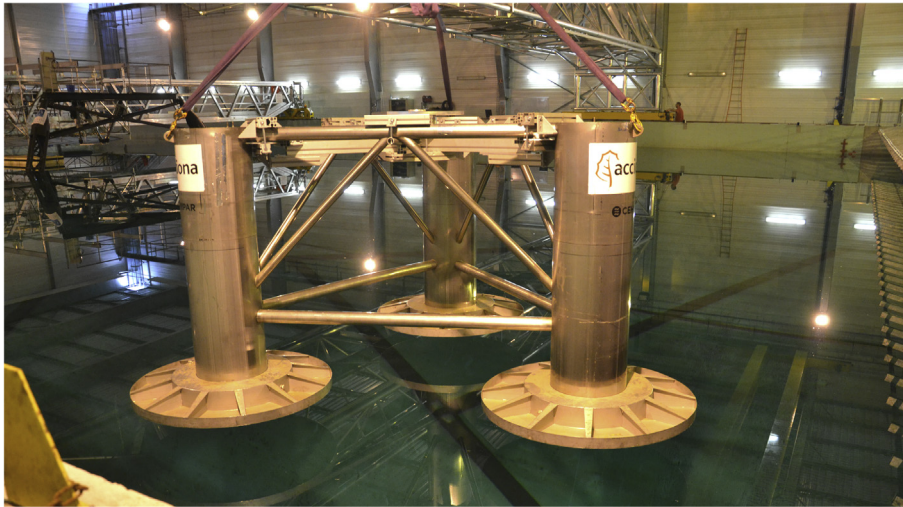


Fig. 5. Semisubmersible platform floater case study model.

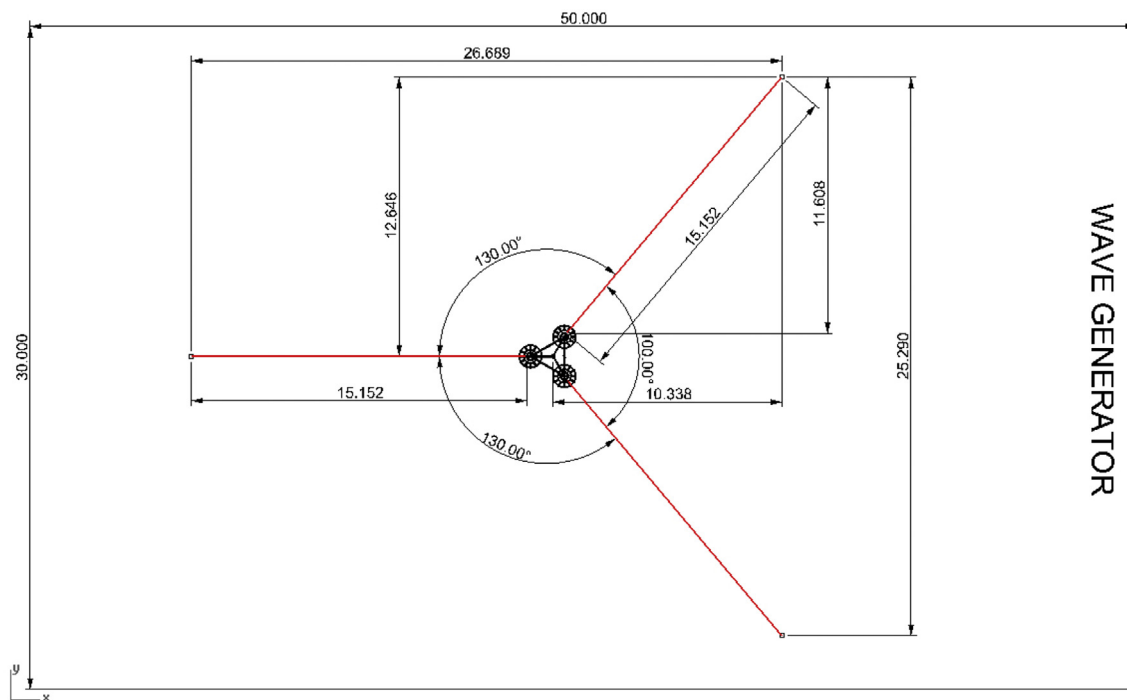


Fig. 6. ECN's wave basin dimensions and mooring configuration.

was basically the same, although the length of the basin is different. CEHIPAR's tank is 152 m long, whereas its width and depth are the same as ECN's (30 m × 5 m). Test campaign at CEHIPAR comprised mainly irregular wave tests. The reason for this choice is that, being three times longer, the tests at CEHIPAR could provide a larger number of resonant slow-drift cycles free from any significant wave reflection effects. Indeed, when trying to assess the slow-drift amplitudes in a model basin, this is a very important aspect; since the second-order forces are estimated indirectly, based on the horizontal excursions of the model, having a large number of resonant cycles is crucial for improving the reliability of the results.

In both campaigns, the motions of the model were recorded by means of optical devices and the tensions on mooring lines were acquired with the use of conventional load cells. Waves in the tank

were calibrated and measured by a number of resistive wave gauges, which were located in different positions within the tanks.

3.3. Numerical model

The numerical prediction of the wave forces was performed using the frequency domain BEM code WAMIT[®] version 6.106 S, including the second-order module.

The floater contains geometric details that must be carefully modeled, especially the heave plates and the hull braces. Regarding the latter, preliminary calculations indicated that the braces do have a significant contribution to the excitation forces and motion RAOs and, for this reason, they should not be disregarded. When modeling the braces, attention had to be paid to the intersections

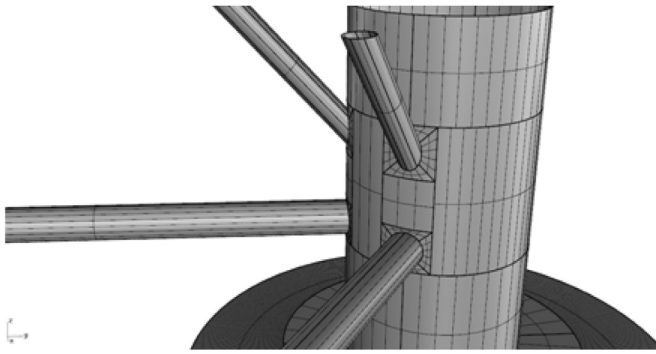


Fig. 7. Mesh details regarding the braces-hull intersections.

with columns, as they present a somewhat complex geometry (see Fig. 7).

Regarding the heave plates, they should, in principle, be modeled as zero thickness elements (dipole elements included in WAMIT), for this option avoids numerical problems when modeling thin structures. However, limitations were found within the second-order module that prevented the use of this option. Therefore, an approximate (thicker) model of the plates was built considering conventional source panels, and an alternative mesh with dipole elements was used only to verify if the first-order results obtained from this approximate model were, in fact, consistent. Since this is an important issue for the numerical model, more details on the adopted procedure are given next.

A first model was done using WAMIT's higher order approach, in which the geometries are described by B-splines and all quantities are continuous inside each patch. Dipole patches were used to model the heave plates, and this mesh is illustrated in Fig. 8.

For the model actually used to compute the second-order forces, the heave plates were represented by conventional source panels as disks of constant thickness. The adjustment of the thickness, however, is not straightforward because a small thickness may lead to numerical problems and one that is too large will impose significant errors concerning the volume of the structure. Different values were tested, after which a thickness of 0.4 m (real scale) was adopted as a reasonable trade-off solution. The analysis was also based on the differences observed for the added masses in surge and heave, when compared to the results obtained with the dipole mesh (typically around 5% for the selected thickness). For illustration purposes only, a comparison of surge and heave added masses using dipole panels and source panels for disks of 0.4 m and 0.8 m

thickness is given in Fig. 9. It can be noticed that the surge added mass does not change appreciably, regardless the thickness adopted. On the other hand, the heave added mass changes more significantly, and it can be noted that the values for the thicker plate are actually closer to those of the dipole panel. However, if the 0.8 m thickness is considered, the displaced volume increases appreciably (almost 500 ton, for a total displacement of 2300 ton). Considering all these aspects, the use of a thickness above 0.4 m was discarded.

The detailed modeling of the braces and heave plates required a higher-order mesh composed of 192 patches. The convergence analysis was performed with several meshes obtained by changing the panel size factor, a straightforward way to change the discretization of the entire geometry. Some of the results of this analysis are illustrated in Fig. 10, in this case for the surge mean drift coefficients, considering meshes with WAMIT panel size parameter equal to 2.5, 5 and 10 m [39]. It should also be stressed that these mean drift forces were computed by pressure integration on the hull, a procedure that is more sensitive to the mesh refinement. A panel size parameter equal to 2.5 m (number of panels equal to 1276) was adopted for all the second-order computations, although, as Fig. 10 indicates, some variations are still observed for wave periods below 5s (very short waves) and around 19s (heave resonance). This trade-off was deemed reasonable, for the full second-order computations are very time consuming and a finer mesh would render the analysis of full QTFs with good frequency resolutions much more difficult.

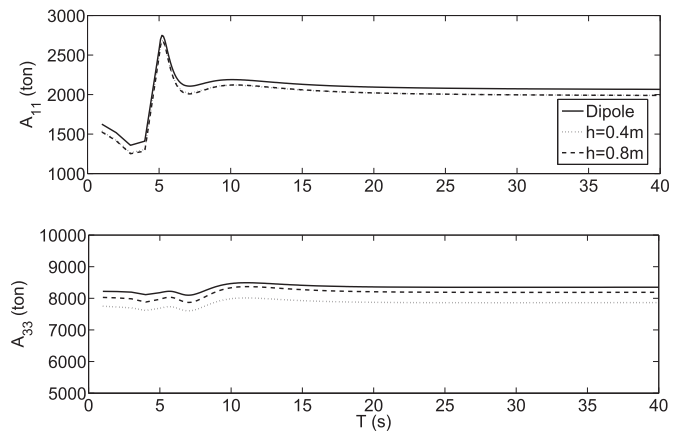


Fig. 9. Comparison of the added masses in surge and heave computed using dipole panels and source panels on disks of 0.4 m and 0.8 m height.

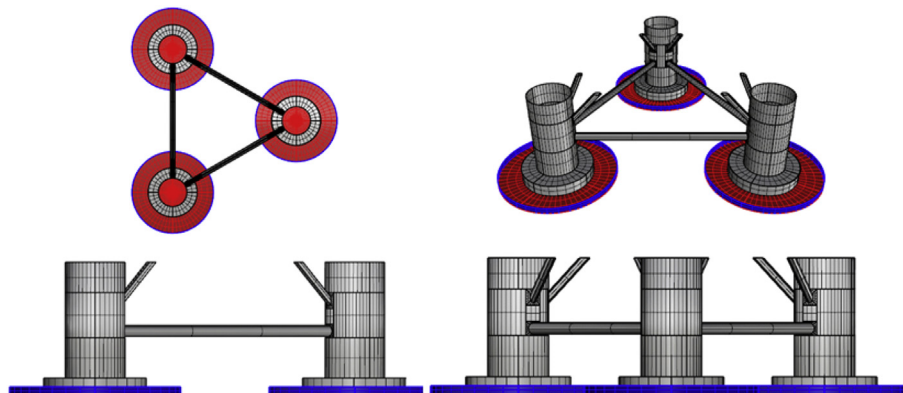


Fig. 8. Higher order mesh of the floating turbine (dipole patches are highlighted in red and blue). (For interpretation of the references to colour in this figure legend, the reader is referred to the web version of this article.)

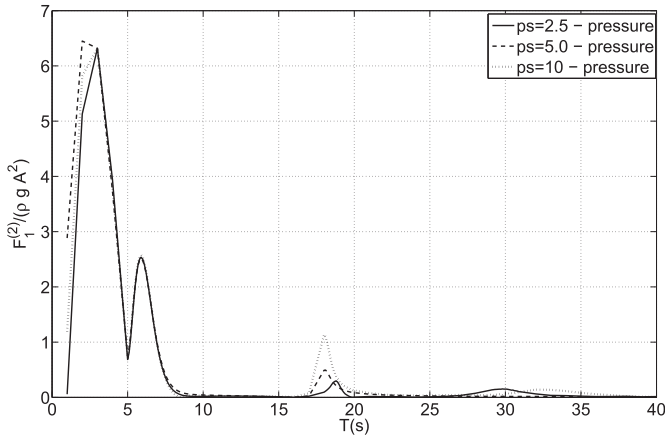


Fig. 10. Comparison of mean drift forces in surge direction for three values of panel size.

Finally, to conclude the discussion on the numerical model, an analysis of the different alternatives that exist to compute the difference-frequency QTF is necessary, for they are also related to the need for the free-surface mesh. As explained in the previous section, the solution of the complete second-order problem, including the second-order potential, requires the mean free-surface boundary to be incorporated to the numerical model. In the present work, the free surface mesh was built considering a total of 21298 panels within a radius of 60 m around the floater (WAMIT's inner radius), as illustrated in Fig. 11.

Nonetheless, it is known that in deep water problems, depending on the geometry involved, some times the second-order potential has only minor contribution in the slow drift forces. If this is the case, an approximation for the computation of this potential in WAMIT may be envisaged, namely disregarding the free-surface forcing terms. Alternatively, in some occasions the second-order potential can be completely neglected without significant loss of accuracy, and the QTFs computed considering only the quadratic terms. The appropriateness of these options is difficult to anticipate, but both of them allow the user to compute the QTF without the need for a free surface mesh, thus saving considerable effort and time. For this reason, a preliminary analysis considering only a few significant QTF terms is always recommendable in order to investigate this possibility. It will be shown, next, that both approximations would indeed be reasonable for the present case study.

For this purpose, and also to investigate the use of Newman's

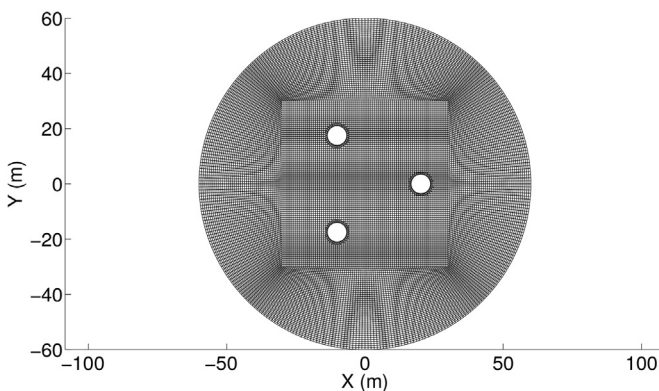


Fig. 11. Free surface mesh assumed in the QTF computations.

approximation, a comparison of the QTF values computed with the full second-order solution (including the free surface mesh) and those obtained according to the different approximations was made for the most relevant frequency pairs involved in the slow-drift dynamics. In the light of the white-noise approach discussed before, it is known that these frequencies are those for which the frequency-difference is equal to the natural frequency of the drift motion. The wave pairs adopted in the analysis can be seen in Fig. 12 over the diagonal that represents the surge natural frequency ($\delta\omega = 0.084$ rad/s), together with the frequency band considered in the computations of the surge QTF.

A comparison of the surge QTF operators obtained if considering only the quadratic terms (without $\phi^{(2)}$), those that include the contribution of the second-order potential computed with and without the free surface forcing terms and, finally, the ones estimated according to Newman's approximation is presented in Fig. 13. One may realize that, in the present case, the second-order potential does not change the QTF appreciably. However, an evaluation of the appropriateness of Newman's approximation can be tricky since observing the results along the whole frequency range, one might conclude that the differences are not pronounced, except for a slight tendency to over predict the QTF values in higher frequencies. Nonetheless, in this analysis it is important to pay

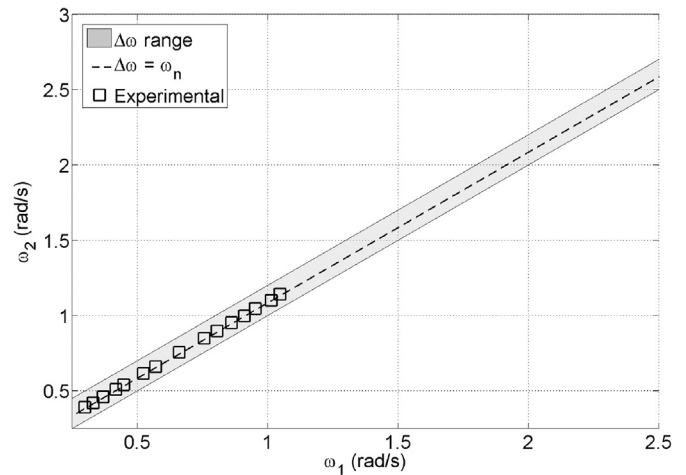


Fig. 12. Wave pairs considered in the QTF study.

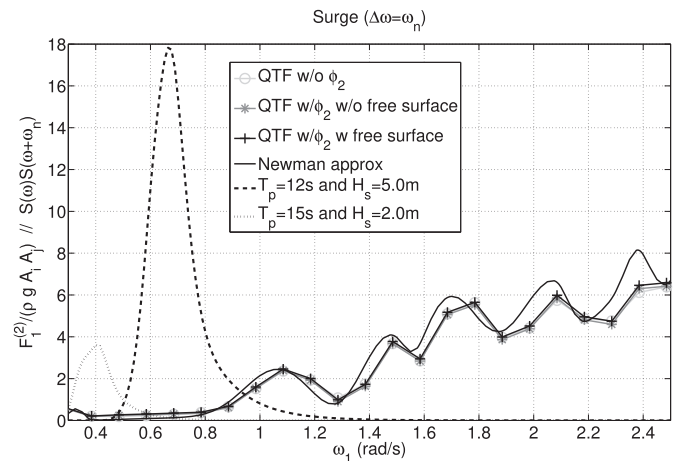


Fig. 13. Surge QTF values considering different approximations and quadratic products involved in the computation of wave group spectrum for two sea conditions.

attention to the range of frequencies in which there will indeed be significant energy in the wave group spectrum. This is why Fig. 13 also presents the quadratic products of the wave spectra involved in the computation of the wave group spectrum for two of the most representative sea conditions considered in the experimental campaign. Observing the energy distributions, it becomes obvious that the most relevant frequency band for the slow motions is typically the one ranging from zero to 1.0 rad/s.

Fig. 14 represents a zoom on the results encompassed within this shorter frequency range, from which one may apprehend that the use of Newman's approximation can lead to an underestimation of the second-forces in the frequencies that will be the most energetic ones. Indeed, this is confirmed by the results presented in the next section.

Finally, it must be stressed that, for all the results that will be presented in the next section, when comparing the numerical predictions and experiments, the QTFs were always obtained using the full second-order solution, meaning the one considering the second-order potential computed with the free-surface forcing terms. However, very similar results would be obtained if the free-surface forcing terms were neglected, or even the entire influence of the second-order potential, a consequence of the small differences observed in Fig. 14.

4. Results

4.1. General

As previously mentioned, the whole experimental campaign comprised decay tests and tests in regular, bichromatic and irregular waves. The main experimental results will be presented hereinafter and comparisons will be made, when applicable, with the numerical simulations. Forced oscillation tests and extreme transient wave tests [40] were also conducted, but they will not be discussed in the present paper since they are not essential for the matter of interest (slow-drift).

Only wave trains with propagation direction parallel to the platform symmetry axis (x -axis in Fig. 6) have been launched. One has to bear in mind that the mooring is oriented so that the most likely extreme waves would come from this direction, making the bow waves the most relevant for the present analysis. Due to the selected heading, sway, roll and yaw motions were negligible in all tests.

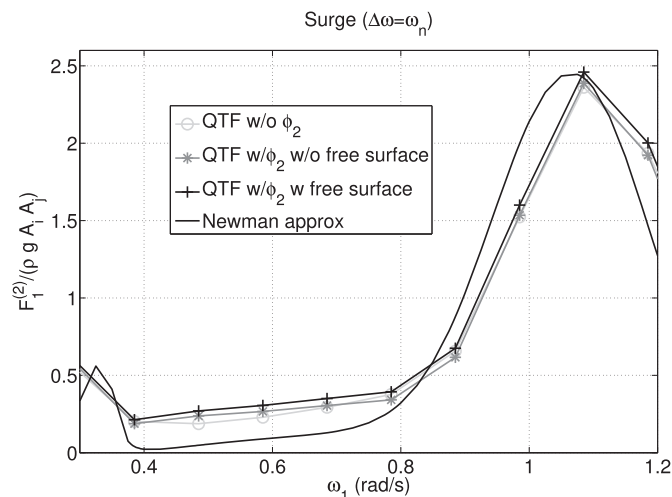


Fig. 14. Surge QTF comparisons (zoom on the frequency range with non-negligible wave group energy).

Results from the decay tests will be discussed first since they provide natural periods and damping characteristics of the system, both necessary to compute and evaluate RAOs, mean drifts, etc.

4.2. Decay tests

When dealing with the slow-drifts of a moored floating system, one always needs to make some sort of prediction of the viscous damping. In fact, the phenomenon concerns a resonant behavior that is significant only because the dynamic system in question is often weakly damped and, consequently, the dynamic amplification induced by the second-order forces is large. If the designer is conducting an analysis based on time-domain simulations in which some sort of non-linear damping model is available (based on the Morison equation, for example), a more “direct” consideration of the damping effects can be made (at least when dealing with slender structures like most FOWTs). However, this is often not the case, especially in the first stages of the design, and quite often the designers must define a preliminary mooring arrangement based exclusively on linear frequency-domain results. In this case, an indirect evaluation of the damping must be made, which involves a linearization of the quadratic viscous forces for a certain representative motion amplitude. This approximation is often based on the designer's experience with similar structures and/or on the results obtained from model tests. In the latter case, the calibration of the equivalent linear damping frequently makes use of results obtained in still water decay tests. Although the flow conditions are obviously not the same as those when incoming waves and other motions are present, the decay tests may provide a reasonable prediction of the damping level that should be expected in wave conditions for deep draft structures.

In the context of the analysis of second-order force models that will be presented in the following sections, a proper estimation of the damping involved in the slow-drift motions is thus very important. For this, some main results obtained in the decay tests performed in different mooring conditions (free floating, horizontal mooring and real mooring) are presented and discussed next. Ahead in the paper, the consistency in using these results (especially those regarding the damping in surge direction) in the slow-drift predictions will be discussed based on the motions recorded in bichromatic and irregular wave tests.

Decay tests were performed in both facilities. As expected, the results were in very close agreement since the model and depth in both basins were the same. For this reason, the results presented in this section refer only to the tests conducted at the ECN wave basin, where a more extensive set of decay tests was made.

4.2.1. Surge motion

Decay tests in surge were performed for both mooring configurations, real (catenary chains) and horizontal mooring (elastic ropes). The outcomes are very similar and the focus will be on the results obtained with the catenary mooring system. Fig. 15 illustrates the results of surge motions for one these tests. The picture on the left depicts the motions obtained during the test, whereas the one on the right presents an estimate of the linearized critical damping factor (ζ) in each amplitude of motion. All values are in full scale.

The mean damped surge natural period for both moorings are close to 75s, indicating that the horizontal stiffness provided by the simplified horizontal moorings is indeed representative of the one provided by the catenary mooring system. The estimated damping levels for the larger amplitudes, say above 100 cm, are around 12% to 15%.

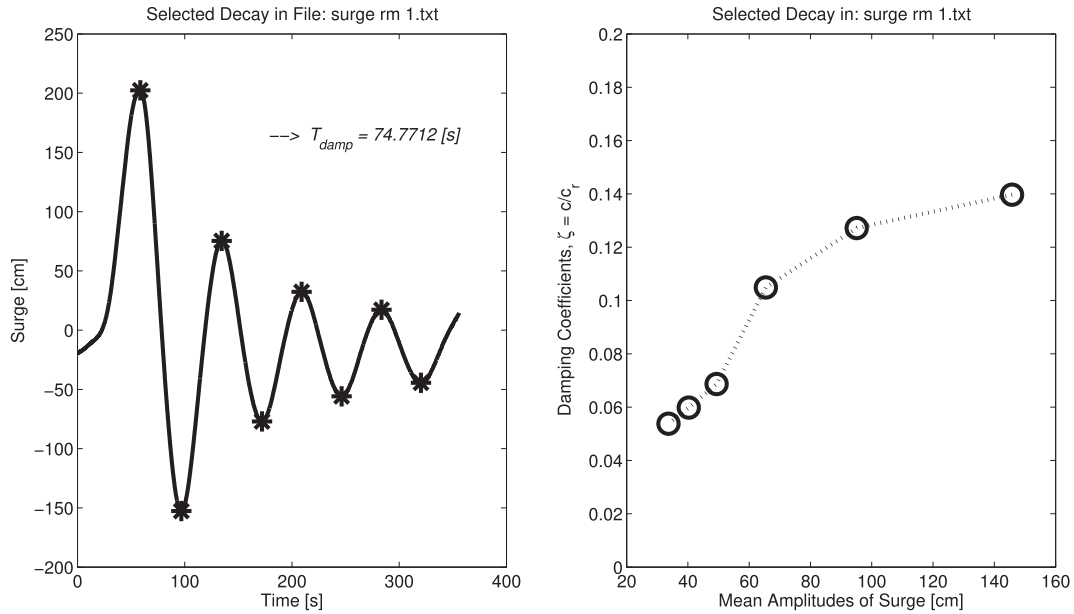


Fig. 15. Sample result for surge decay test in real mooring configuration (left) and estimates of critical damping factor (right).

4.2.2. Heave and pitch motions

Prior to the connection of the moorings, some decay tests in heave were made. Due to the large heave plates installed at the bottom of each column, it is known that influence of the moorings in the vertical motion is negligible. Results are illustrated by Fig. 16, in the same pattern of those presented in the last section. The damped heave natural period is estimated to be around 19s, and the critical damping level for the larger amplitudes, say above 20 cm, is found to be in the range of 6%–8%.

Decay tests for pitch were performed for both catenary and horizontal moorings. Again, the results were in good agreement, attesting that the pitch damping is also dominated by the flow separation on the heave plates. Fig. 17 presents a sample result obtained in a test with the real mooring configuration. The mean

damped pitch period is around 25s.

The mean values obtained for the natural periods of each motion (surge, heave and pitch) were already presented in Table 1. The damping levels estimated from the decay tests will be discussed again in the next sections, when the motions of the floater in regular and irregular waves are analyzed.

4.3. First-order results: RAOs from regular and bichromatic wave tests

Experimental values for the motion RAOs of the floater were obtained from both regular and bichromatic wave tests. The regular wave tests were carried out for periods, T , between 6 and 20s and wave heights, H , of 2 and 4 m. For illustration purposes, an excerpt

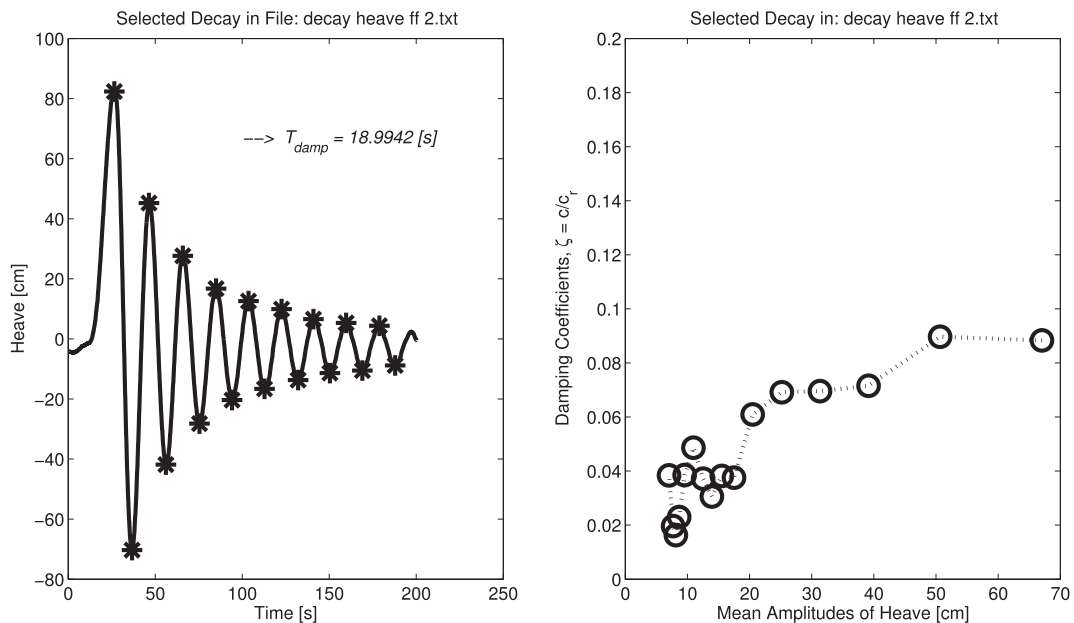


Fig. 16. Sample result for heave decay tests in free floating condition (left) and estimates of critical damping factor (right).

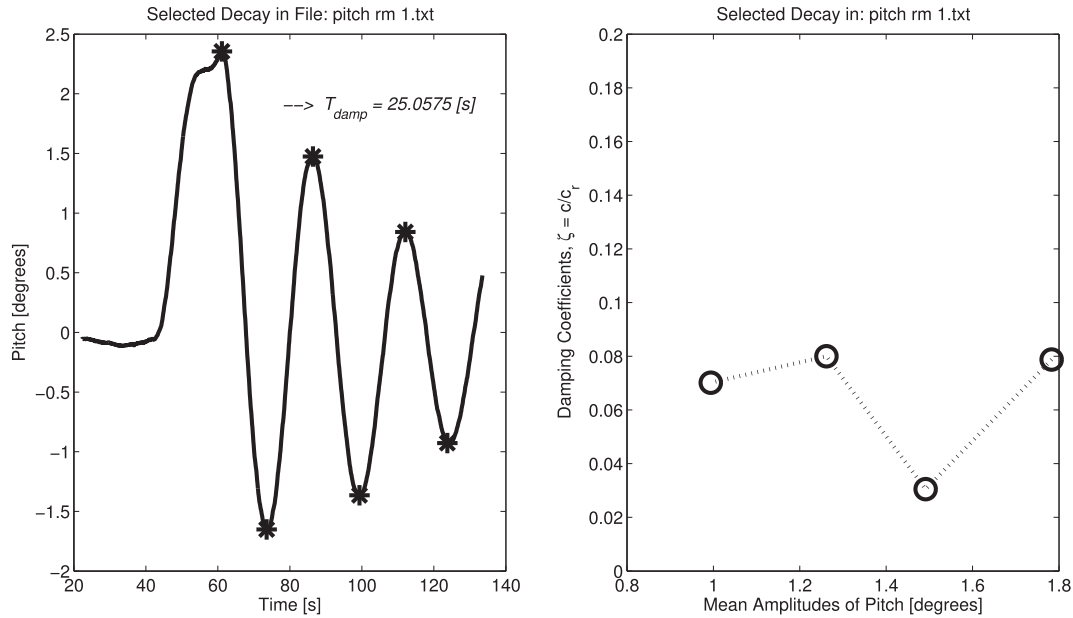


Fig. 17. Sample result for pitch decay tests in real mooring condition (left) and estimates of critical damping factor (right).

of one of the records depicting the measured surge, heave and pitch motions is shown in Fig. 18. For the real mooring configuration only regular waves with $H = 2.0$ m were tested.

In order to facilitate the reproducibility of present results, the parameters adopted for all bichromatic wave tests are shown in Table 3. All conditions were tested for the horizontal mooring setup, while for the real mooring configuration only the cases with id from 18 until 33 were considered. An example of motion records obtained in the bichromatic tests can be seen in Fig. 19. One may readily see that, besides the motions in the wave frequencies, there is a slow oscillation of the model in a frequency that corresponds to the frequency difference $(\omega_1 - \omega_2)$.

The analysis performed for computing the RAOs assumed the motion signals as sinusoidal since one is only interested in the first-order motions. The signals were first smoothed by means of an average filter and the time span considered in the analysis carefully selected in each case to exclude any transient motions. A simple Fourier filter was applied in order to remove the energy in frequencies that were not the ones of interest in each case (transient effects, slow-drifts, etc.) and the time series was then reconstructed

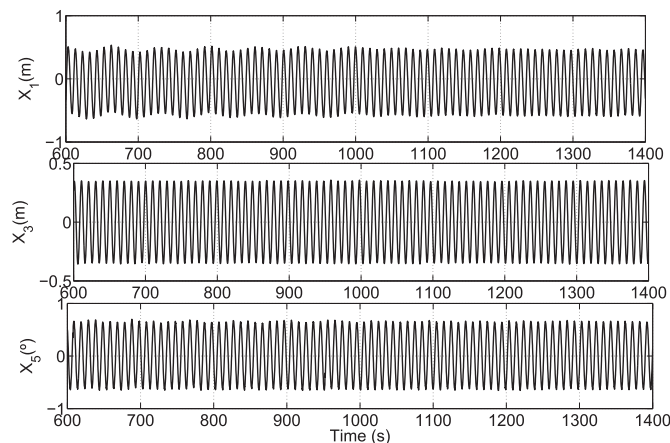


Fig. 18. Example of time series of motions in a regular wave test ($T = 10$ s, $H = 2$ m).

Table 3
Bichromatic waves considering in the tests.

ID	H1 (m)	T1 (s)	H2 (m)	T2 (s)	ΔT (s)
BIC 1	5.63	17.0	3.46	12.2	42.9
BIC 2	4.39	15.0	2.45	10.2	32.1
BIC 3	4.39	15.0	2.89	11.1	42.9
BIC 4	2.80	9.5	1.88	7.8	42.9
BIC 5	4.39	15.0	1.50	6.9	12.9
BIC 6	2.13	8.3	1.50	6.9	42.9
BIC 7	1.88	7.8	1.11	6.0	25.7
BIC 8	1.50	6.9	1.11	6.0	42.9
BIC 9	1.67	7.3	1.01	5.7	25.7
BIC 10	1.35	6.6	1.01	5.7	42.9
BIC 11	1.88	7.8	0.93	5.5	18.4
BIC 12	1.50	6.9	0.93	5.5	25.7
BIC 13	1.22	6.2	0.93	5.5	42.9
BIC 14	1.67	7.3	0.85	5.2	18.4
BIC 15	1.35	6.6	0.85	5.2	25.7
BIC 16	1.11	6.0	0.85	5.2	42.9
BIC 17	1.50	6.9	0.79	5.0	18.4
BIC 18	5.63	17.0	4.32	13.6	68.0
BIC 19	5.27	15.0	3.54	12.3	68.0
BIC 20	2.80	9.5	1.62	8.3	68.0
BIC 21	2.13	8.3	1.27	7.4	68.0
BIC 22	1.88	7.8	1.14	7.0	68.0
BIC 23	1.50	6.9	0.92	6.3	68.0
BIC 24	1.67	7.3	1.02	6.6	68.0
BIC 25	1.35	6.6	0.84	6.0	68.0
BIC 26	1.22	6.2	0.77	5.7	68.0
BIC 27	1.11	6.0	0.70	5.5	68.0
BIC 28	2.83	11.0	2.10	9.5	68.0
BIC 29	3.37	12.0	2.44	10.2	68.0
BIC 30	4.59	14.0	3.16	11.6	68.0
BIC 31	5.64	19.0	5.16	14.9	68.0
BIC 32	2.82	19.0	5.16	14.9	68.0
BIC 33	3.44	21.0	6.03	16.0	68.0

using the inverse Fourier transformation. The same procedure was performed for the bichromatic waves in order to segregate both frequencies, although some overlap may be present for some specific wave conditions. The standard deviation was computed from the smoothed signal after the Fourier filter was applied, from which the motion amplitude for each degree of freedom was obtained.

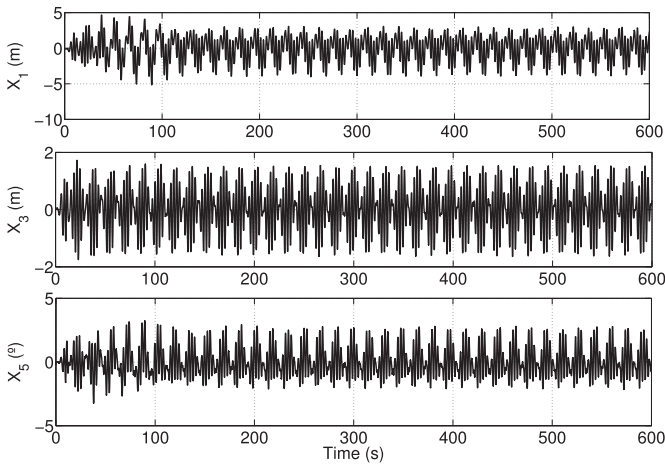


Fig. 19. Example of motions recorded in bichromatic wave tests ($\omega_1 = 0.86$ rad/s, $\omega_2 = 0.95$ rad/s, $H_1 = 1.67$ m, $H_2 = 1.25$ m).

RAOs for surge, heave and pitch motions obtained with the floater moored horizontally are presented in Fig. 20, together with the numerical predictions obtained from WAMIT. In this case, regular (monochromatic) wave tests were carried out with wave heights of 2 and 4 m. The comparison shows that there is no evidence of significant non-linearities in motions within this range since motions in both wave heights provided similar amplification factors. Nonetheless, a poor agreement for the heave motion in its resonant range (close to $T = 19$ s) is noticeable. This, however, is not unexpected in the analysis of a structure composed of slender elements as this one (see, for instance, Ref. [41]), for the flow induced by the waves of larger periods will be characterized by a relatively large KC number. As a consequence, viscous drag effects will have a more significant role for these wave periods and, of course, the impact on the motions will be more evident within the resonance range. In addition, it should be noted that the waves with a period of 20s have a length of approximately 500 m in infinite depth (almost 25 m in model scale), which is already larger than the distance between the model and the wave generator (setup can be seen in Fig. 6). It seems plausible that the progressive wave may not yet have reached a steady profile when it reaches the model, and this can be another source of discrepancies for the very large

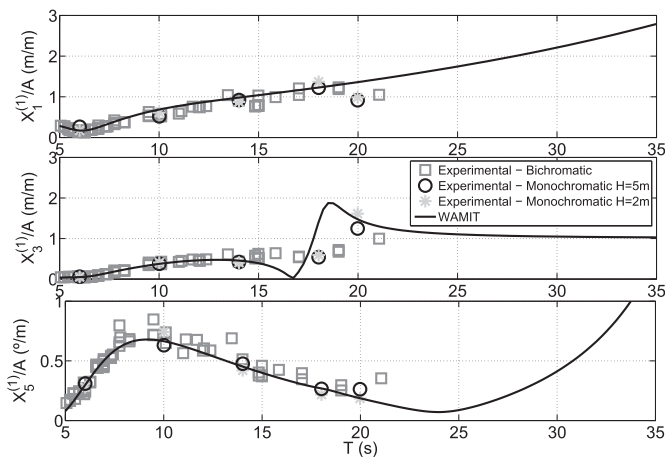


Fig. 20. RAOs for surge, heave and pitch motions obtained from experiments with horizontal moorings. Includes results from tests with regular (monochromatic) waves with two different heights and bichromatic waves. Numerical predictions from WAMIT are also presented for the sake of comparison.

periods. Nonetheless, it must be emphasized that the agreement obtained for the surge RAOs is quite fair for almost all wave periods, except, again, for some small discrepancies above 20 s. Since the surge drift motions are the main focus of the present work, the agreement observed for the first-order results is deemed satisfactory.

The same set of RAOs are presented in Fig. 21, now for the model with catenary mooring chains. The agreement between numerical and experimental results is similar to the one observed for the horizontal moorings, except for the discrepancies on the pitch motions in large wave periods. It should be noticed that these discrepancies happen mainly for the bichromatic wave tests, and are much smaller for the regular waves. The reasons for this are connected to the errors in the heave motions (it is easy to notice that they are also larger in the bichromatic wave tests). With the non-symmetric catenary moorings, there is a coupling effect between heave and pitch motions, implying that errors in the heave amplitudes also impose errors in pitch. As mentioned above, the discrepancies are related to the larger KC numbers, which also increase with the wave amplitude. For the larger wave periods, the wave amplitudes adopted for the bichromatic waves are much larger than the one adopted in the regular wave tests ($H = 2$ m), reaching 6 m for the waves with a period of 21s (see Table 3). The larger amplitudes surely contribute to the larger discrepancies in the results of the bichromatic tests. Moreover, other sources of error may also have an impact, such as the limitations related to the long waves generation already mentioned above. In this case, even the simplified (linearized) mooring stiffness model required by the frequency-domain solution may contribute to the differences, for this model is only reasonable for small displacements. However, apart from the discrepancies noted for the pitch motions, the agreement in the surge RAO for the catenary moorings is once again fair, attesting that the numerical model was able to capture well the dynamics in surge.

Finally, in order to conclude the assessment of the first-order results, it is important to emphasize the fact that the agreement in surge motion is not significantly impacted by pronounced discrepancies in pitch. This confirms that the effects of pitch on the surge motions (due to the surge-pitch coupling) are indeed small. As mentioned in Section 2, this assumption is important for the analysis of the slow-drift motions using the white-noise approach.

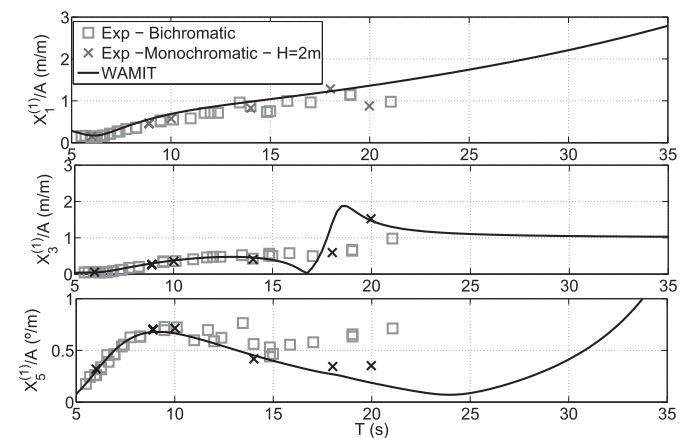


Fig. 21. RAOs for surge, heave and pitch motions obtained from experiments with catenary moorings. Includes results from tests with regular (monochromatic) waves and bichromatic waves. Numerical predictions from WAMIT are also presented for the sake of comparison.

4.4. Second-order results

Next, all the experimental results that involve low-frequency second-order effects are analyzed and compared to the predictions obtained with the numerical models discussed in Section 3. First, the predictions of mean drift forces are evaluated, using for this the mean excursions and the mean tensions on the horizontal mooring lines recorded during the regular wave tests. Next, slow drift motions observed in bichromatic waves are used as a basis for assessing the low-frequency drift forces for the different pairs of frequencies that were tested. In this analysis, a discussion on the slow-drift damping is also presented. Finally, the motions observed in several conditions of irregular waves with different wave heights and peak periods are analyzed and compared to those predicted by the numerical models, and the performance of the different approximations considered for computing the QTFs is discussed.

4.4.1. Mean drift analysis from regular waves

Few comparisons of mean drift forces for a typical wave frequency range are available in literature (e.g. Ref. [42] obtained experimental measurements of drift forces for a TLP). The reason for this scarcity is that the mean drift forces are small compared to first-order ones and thus they are quite difficult to measure with reasonable accuracy. Having the tensions monitored in the present setup, an attempt has been made considering two different methods, discussed next.

The surge natural period can be evaluated from expression (9), where M is the mass displacement, A_{11} is the added mass computed for the natural frequency in surge (estimated with WAMIT) and K_x denotes the surge stiffness provided by the moorings. Considering the natural period obtained experimentally, the solution of this equation provides an estimate for K_x , which can be subsequently multiplied by the mean excursion in surge obtained from the motion records for an estimation of the mean drift force according to Eq. (10). In this equation, $\bar{X}_1^{(2)}$ denotes the mean excursion in surge, which is a second-order quantity. This procedure will be referred to as Method 1.

$$T_1 = 2\pi \sqrt{\frac{M + A_{11}}{K_x}}. \quad (9)$$

$$F_1^{(2)} = K_x \cdot \bar{X}_1^{(2)}. \quad (10)$$

The second method adopted (Method 2) uses the tensions recorded on the mooring lines, which can be projected in the x direction and summed up to provide the mean surge force. The angles between the mooring lines can be obtained from the mooring arrangement in Fig 6. The total mean drift force can thus be computed from Eq. (11), where $\bar{F}_1, \bar{F}_2, \bar{F}_3$ are the mean values of the tensions on the corresponding mooring lines.

$$F_1^{(2)} = \bar{F}_1 \cos(40.2) + \bar{F}_3 \cos(39.3) - \bar{F}_2. \quad (11)$$

$\bar{F}_1, \bar{F}_2, \bar{F}_3$ must be carefully calculated from measurements, considering the pretensions adopted in the tests.

Considering the tests performed with the catenary mooring system, the comparison between the mean drift forces estimated with both methods and those predicted by WAMIT can be seen in the top panel of Fig. 22. The agreement is considered reasonable, especially taking into account that second-order quantities are significantly smaller than the first-order ones and that accurate measurements of these quantities are not easy to perform. Mean drift displacements are also provided in the bottom panel of Fig. 22.

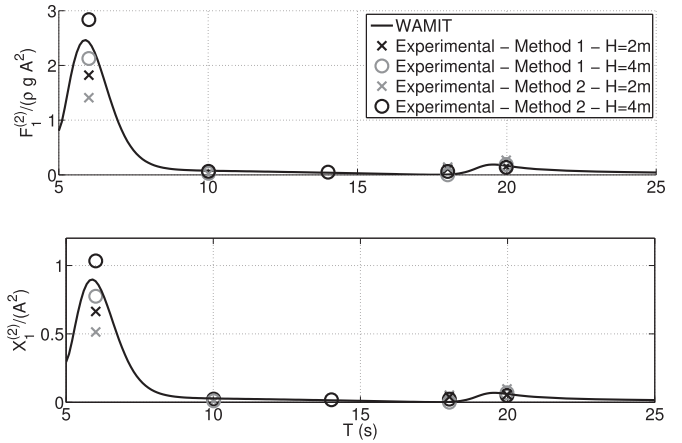


Fig. 22. Surge mean drift forces for regular waves under real mooring. Displacements (bottom). A is the wave amplitude, g gravity, ρ water density.

The results obtained for the horizontal mooring configuration were very similar and, for this reason, they are not presented.

4.4.2. QTFs from bichromatic wave tests

Bichromatic wave tests comprised the combination of two regular waves with slightly different frequencies (ω_1, ω_2), as indicated in Table 3. The main purpose of testing the floating platform in bichromatic waves was to derive estimates of the slow-drift forces from the amplitudes of drift observed in each test. For reasons that were already mentioned before, most of the tests were done for frequency pairs whose difference $\Delta\omega$ was close to the platform's natural frequency in surge.

At this point, it is important to remind the reader that previous bichromatic tests had been made with the same floater model but in fixed condition, as reported in Ref. [21]. The advantages of employing a captive model for verifying the second-order computations are clear, for in the fixed-model setup the wave forces on the hull can be measured in a direct manner. In this way, QTF values measured experimentally with a dynamometer could be straightforwardly compared to the corresponding numerical predictions for different pairs of frequencies (ω_1, ω_2). The results showed a very reasonable agreement for most situations, although the numerical predictions had a slight tendency to underestimate the second-order forces in some situations. However, the use of a fixed model also brings a significant drawback because the forces measured in this condition may be quite different from the ones that occur when the model is free to move in waves. The motions of the platform change the quadratic pressure on the hull and also impose variations of the wetted surface. Both matters may have a significant impact on the slow-drift forces.

For this reason, the aforementioned previous experimental study was complemented by the present bichromatic tests, performed at the ECN wave basin with the model moored by the catenary chains. On the negative side, this set-up turns the evaluation of the diffraction forces more difficult, introducing damping forces as the floater drifts on the horizontal plane. As a consequence, the assessment of the accuracy of the QTF computations must be performed indirectly, from the amplitudes of drift recorded for each frequency $\Delta\omega$. Being a resonant problem, this assessment also depends on the consideration of the motion damping.

An example of the motions observed in the bichromatic wave tests was presented in Fig. 19, in which it can be easily seen that, besides the motions in the wave frequencies, there is a slow oscillation of the model in the frequency difference ($\omega_1 - \omega_2$).

For the analysis of the QTF, the second-order RAOs for surge motion ($|X_1|/A_1 A_2$) were derived for each frequency pair and the result is depicted in Fig. 23. In this figure, the RAOs are plotted against the first wave frequency (ω_1 , values in full scale). All the results correspond to the same frequency difference, which is close to the surge natural frequency of the floating platform ($\Delta\omega = \omega_n$). Fig. 23 also presents a set of second-order surge RAOs obtained from WAMIT with the full second-order QTFs and considering different levels of surge damping. For the computation of these RAOs, the damping factor was kept constant for all the other degrees of freedom.

The analysis of the results indicates that considering an equivalent linearized damping factor in the range between 10% and 15% of the critical damping leads to a fair agreement between experimental and numerical predictions of the slow-drift motion amplitudes. This is more evident for frequencies ω_1 above 0.8 rad/s (roughly meaning wave periods below 8.0s), when the wave reflection on the hull becomes more pronounced and, consequently, the drift motions tend to increase. It is true that discrepancies seem to rise for frequencies above 1.0 rad/s, but this can be justified by the larger uncertainties involved in the analysis of these cases. In fact, it must be reminded that, with shorter waves, also the mean excursions increase in this frequency range (see Fig. 22), making the effectiveness of the simplified models adopted to represent the mooring effects in Eqs. (10) and (11) less certain. The variability in the high frequency results is thus connected to level of uncertainty also observed in the peak values of the mean drifts in Fig. 22, which happen for similar wave periods.

It should be mentioned that the amplitudes of slow-drift excursions for most of the bichromatic tests with $\omega_1 > 0.8$ rad/s are over 1 m (in full scale). It is interesting to observe that the damping range predicted for such amplitudes reported in Section 4.2.1 (between 10 and 15%) is in fact consistent with the one that guarantees a good adjustment between numerical predictions and bichromatic wave tests. This fact confirms that the aforementioned damping range is also representative for the problem of the floater in waves and, for this reason, it will be considered in the analysis of the irregular wave tests.

4.5. Response spectra in irregular wave tests

Tests with the floater moored by the catenary mooring system in several irregular wave conditions were performed at the CEHIPAR wave basin. Peak periods T_p ranged from 9.0s to 16s and were

combined with different values of significant wave heights H_s . Power spectra were generated according to a conventional JONSWAP model.

In general, the lower the peak period, the more intense the slow-drift amplitudes measured in the tests. For this reason, the results in this section will be presented with waves sorted in a descending order of T_p .

As mentioned before, only bow wave conditions were tested, and thus the results will comprise only surge, heave and pitch motions (it was verified that all other motions were indeed negligible). The analysis of the results is based on the agreement between experimental motion spectra (derived from the motion records) and those predicted by the numerical model (computed according to Eqs. (5)–(7)). Comparisons are made both at a spectral level and considering significant statistical parameters.

Again, since the analysis depends on the motions of the floater, the choice of the damping level to be considered in the numerical model becomes a critical issue, especially for the computation of the slow-drift amplitudes. With this in mind, all the numerical predictions concerning the surge motions will be presented for two different values of linearized (external) damping, namely $\zeta = 10\%$ and $\zeta = 15\%$. This is done in order to provide a typical range of fluctuation of the numerical predictions. As already discussed, these damping limits are consistent with the estimations obtained from decay tests (Section 4.2) and bichromatic wave tests (Section 4.4.2). Heave and pitch motions were both computed considering a damping factor of 7%.

Moreover, predictions of motion spectra were always computed considering the wave power spectrum derived from the wave-probe records obtained in the wave calibration tests, instead of employing the theoretical JONSWAP spectrum based on the required (H_s , T_p). By following this procedure, eventual discrepancies between theoretical and experimental wave spectra will not affect the level of agreement observed between predicted motions and those effectively measured in the tests.

First-order motion spectra were obtained with two different approaches: in the first one, the first-order RAOs were computed in WAMIT considering all couplings between motions already discussed in Section 2; in the second approach, on the other hand, the motion spectrum for each d.o.f. was computed using the RAOs obtained when all couplings are disregarded. Results for both approaches are presented in Figs. 24–26. As discussed before, these effects have a somewhat large influence on the first-order pitch motions. For surge and heave, nonetheless, the improvement that is obtained when including the coupling effects is much smaller. One should remind that the uncoupled approach is used for computing the second-order force spectrum with the white-noise approximation.

In addition, an explanation regarding the different models adopted for computing the slow-drift motions is necessary. The results were obtained with three different models, namely: the full second-order QTF matrix obtained with WAMIT (indicated by “Full QTF” in the figures); Newman’s approximation (indicated by “Newman app.” or NA) and white-noise approach (denoted by “WN”). The hypothesis involved in these two approximations and their theoretical basis were discussed previously in Section 2.

For the full second-order computations, the QTFs were computed for a range of difference-frequencies ($\delta\omega = \omega_1 - \omega_2$) between 0.025 rad/s and 0.20 rad/s (corresponding to wave group periods varying roughly from 30s to 250s).

The second-order surge spectra computed with the full second-order QTFs and Newman’s approximation are shown in Figs. 24–26, respectively for seas with peak periods T_p of 10, 12 and 15s. These wave conditions were selected as being representative of the whole range of irregular waves tested.

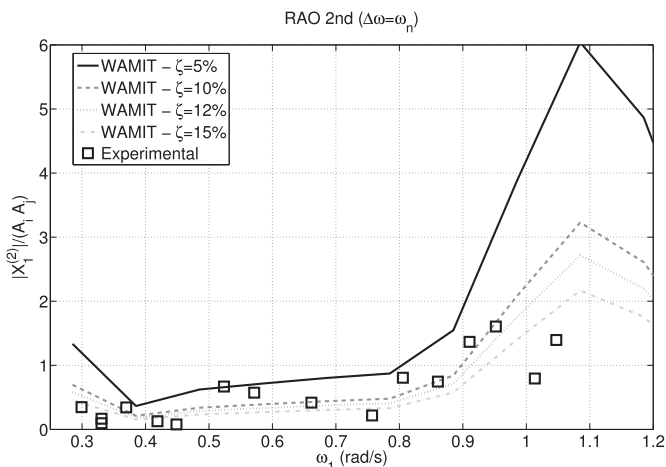


Fig. 23. Second-order surge RAO obtained from bichromatic wave tests and numerical estimations considering different (linearized) damping levels.

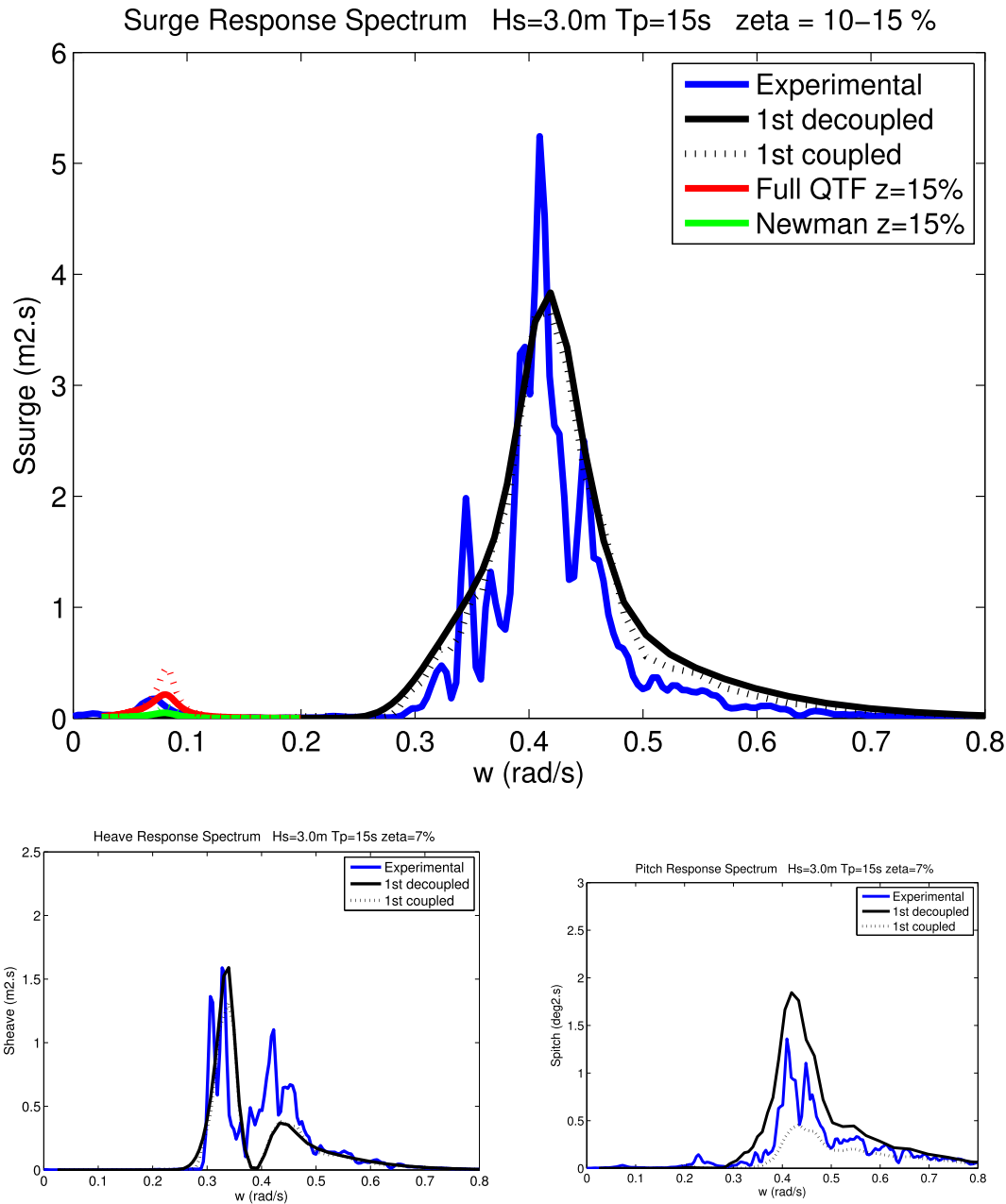


Fig. 24. Motion Spectra for surge (top), heave (left) and pitch (right). $H_s = 3.0$ m, $T_p = 15$ s. Experimental spectrum (blue); First-order spectra: decoupled analysis (black), coupled analysis (black dashed). Second-order surge spectra: from QTFs (red), from Newman's approximation (green) ($\zeta = 10\%$ dashed lines, $\zeta = 15\%$ solid lines). (For interpretation of the references to colour in this figure legend, the reader is referred to the web version of this article.)

It is clear from the pictures that the slow-drift motions become much more pronounced as the peak period decreases from 15s (Fig. 24) to 10s (Fig. 26). Moreover, the variability obtained in the slow-drift spectra when considering a typical range of damping from 10% (dashed lines) to 15% (solid lines) is also noticeable in the figures, illustrating the intrinsic uncertainty that is always involved when dealing with the problem in the frequency-domain (and thus depending on linearized damping estimates). Regarding the agreement between experimental and predicted second-order spectra, the results indicate that the use of Newman's approximation leads to slow-drift energies that are somewhat smaller if compared to those predicted with the full QTFs.

Although the spectral analysis illustrates the dynamics of the problem and the agreements obtained, the comparisons are

certainly more objective if based on the spectral moments m_0 and on the amplitudes computed from them. Table 4 presents the mean amplitudes of first and second-order surge motions, computed as $A = 2\sqrt{m_0}$, for the corresponding parts of each spectrum. The table also presents the main parameters of the wave spectrum for each test (both required and estimated from the experimental wave records) and a representative wave steepness based on the values of H_s and T_p . One should notice that only the amplitudes calculated with the coupled model, which is supposed to be more accurate, are included in the table.

The results on Table 4 confirm that the slow-drift tends to increase as the peak period decreases. In general, the rise in the amplitude values derived from the motion records ($A_{2_{exp}}$) is followed closely by the numerical predictions obtained both from the

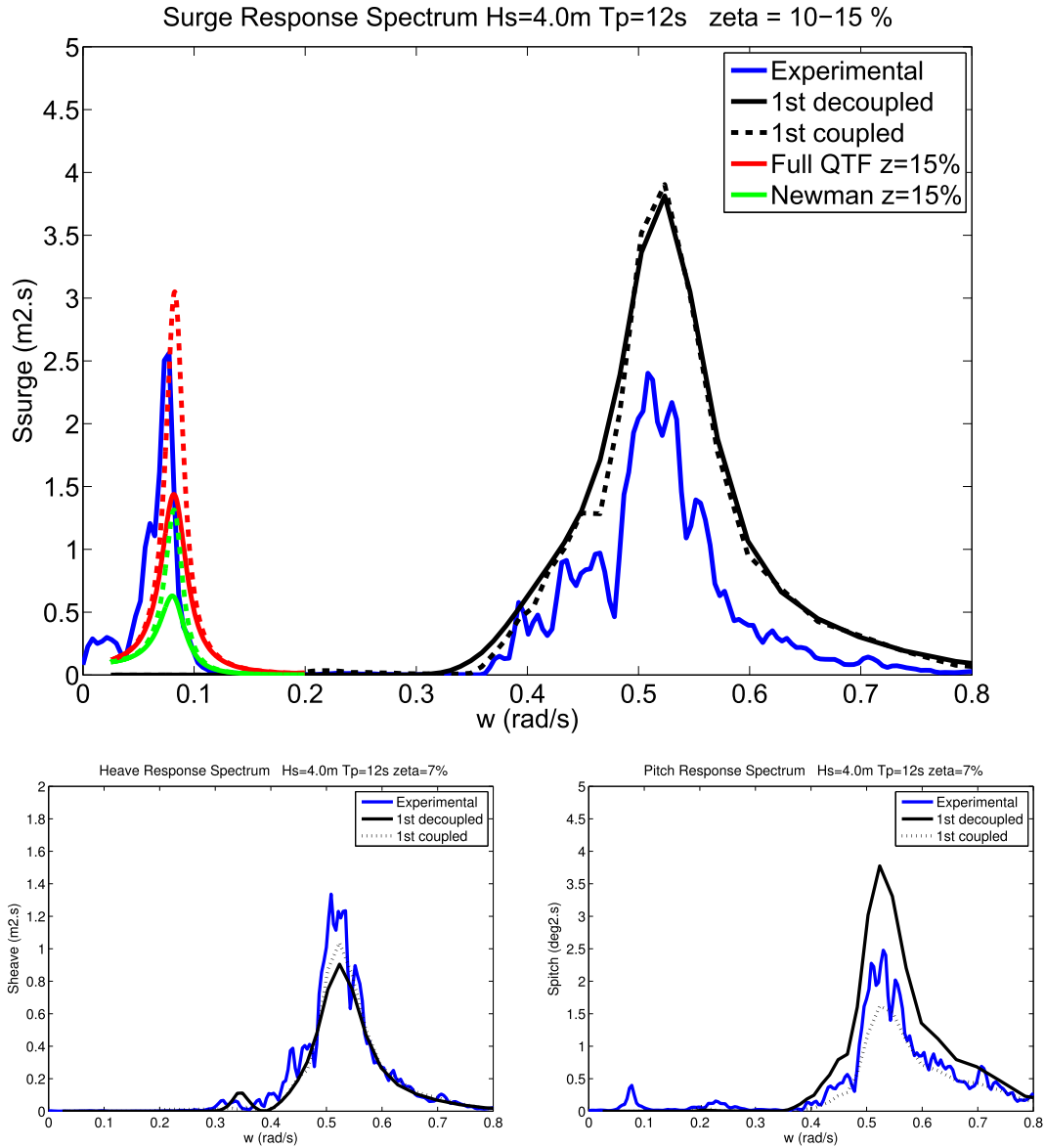


Fig. 25. Motion Spectra for surge (top), heave (left) and pitch (right). $H_s = 4.0$ m, $T_p = 12$ s. Experimental spectrum (blue); First-order spectra: decoupled analysis (black), coupled analysis (black dashed); Second-order surge spectra: from QTFs (red), from Newman’s approximation (green) ($\zeta = 10\%$ dashed lines, $\zeta = 15\%$ solid lines). (For interpretation of the references to colour in this figure legend, the reader is referred to the web version of this article.)

full QTF and with the use of Newman’s approximation. For the latter, however, one may realize that the estimations are consistently below those derived from the QTFs. For the floater under analysis, therefore, this approximation may not be the best choice for the mooring design, for it tends to generate less conservative results.³

Another aspect of the results in Table 4 deserves attention: Actually, one may realize that the errors in the estimations of first-order surge amplitudes also seem to increase as the wave steepness increases. This may happen due to variations in the mooring effects associated with larger mean drifts and surge motions, which are not correctly captured on a simplified linear analysis. Errors might also be connected to the rise in KC numbers for the larger wave

amplitudes and, therefore, to possible viscous effects on the hydrodynamic exciting forces that are not accounted for in the diffraction-radiation analysis.

The larger discrepancies observed on the first-order results for the larger waves certainly raise some doubts regarding the uncertainty in the comparisons of the slow-drift motions. However, it must be emphasized that there is no evidence that effects such as the ones mentioned above might have changed the second-order results significantly. On the contrary, the variation of slow-drift amplitudes observed in the tests seems to follow the theoretical predictions closely, as one may deduce from Fig. 27. This figure depicts the mean slow-drift amplitudes as a function of the wave peak period for each test and the results attest that, in general, the behavior of the second-order motions is consistent with the expectancies (one should notice that the x-axis in this figure merely lists the different tests in a descending order of T_p , and some values of peak periods were repeated in tests done with different wave heights).

³ It is interesting to notice that these results corroborate the previous analysis presented in Ref. [21], based on experimental data obtained when the same model platform was subjected to captive model tests in CEHIPAR.

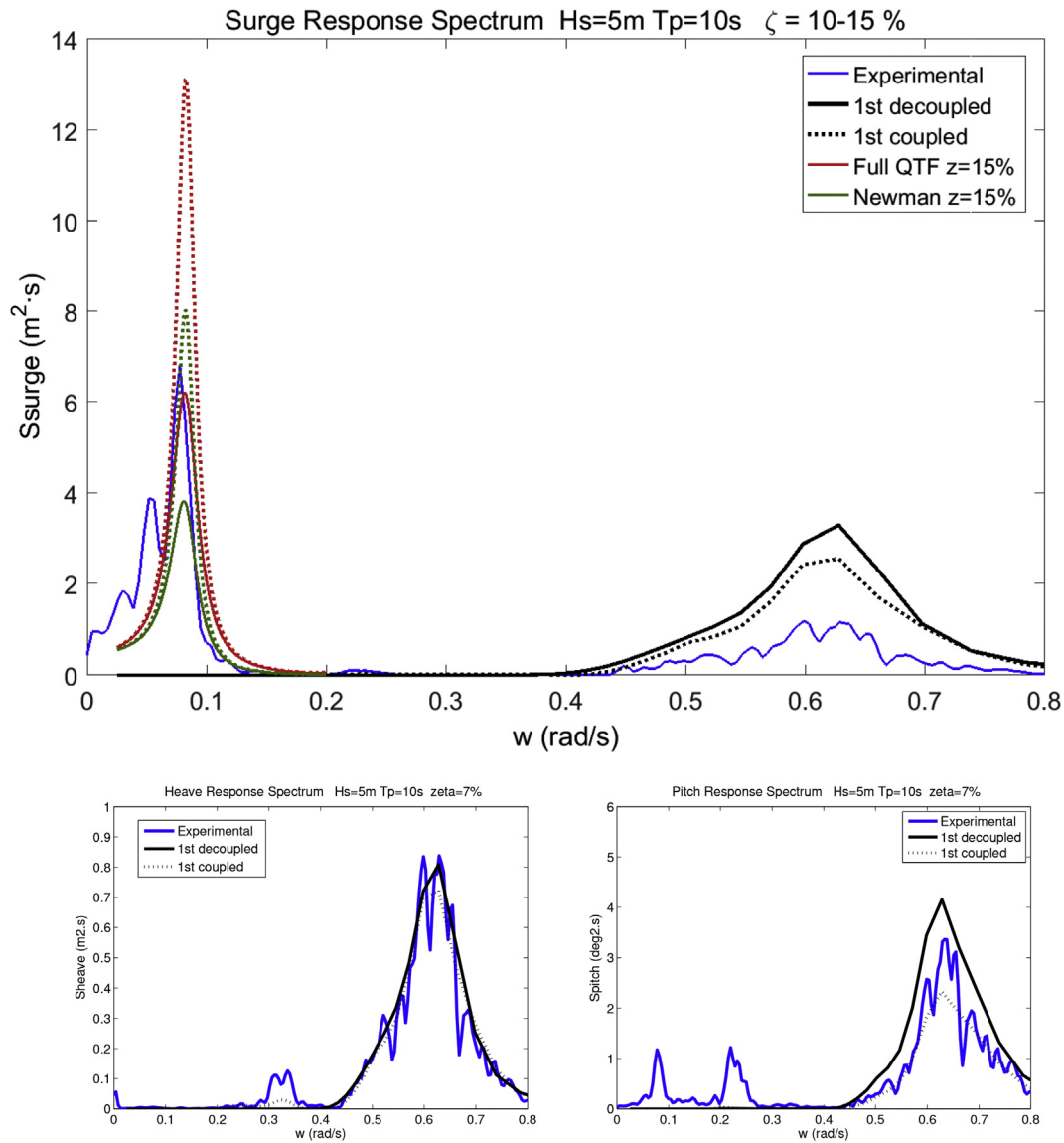


Fig. 26. Motion Spectra for surge (top), heave (left) and pitch (right): $H_s = 5.0$ m, $T_p = 10$ s. Experimental spectrum (blue); First-order spectra: decoupled analysis (black dashed), coupled analysis (black dotted); Second-order surge spectra: from QTFs (red), from Newman's approximation (green) ($\zeta = 10\%$ dashed lines, $\zeta = 15\%$ solid lines). (For interpretation of the references to colour in this figure legend, the reader is referred to the web version of this article.)

Table 4
Mean surge amplitudes obtained for the different irregular wave tests (SI units). First-order amplitudes (A1) obtained from experimental records ($A1_{exp}$) and from WAMIT's RAOs ($A1_{num}$). Second-order amplitudes (A2) obtained from experimental records ($A2_{exp}$) and from numerical models considering the QTFs and Newman's approximation (NA).

Hs	Tp	Steep (%)	Hs _{exp}	Tp _{exp}	A1 _{exp}	A1 _{num}	A2 _{exp}	A2 _{num} QTF		A2 _{num} NA	
								z = 15%	z = 10%	z = 15%	z = 10%
2.5	16	0.63	2.28	15.51	0.97	1.04	0.14	0.12	0.14	0.07	0.08
3.0	15	0.85	2.96	15.19	1.13	1.28	0.17	0.19	0.23	0.09	0.11
3.0	14	0.98	2.90	13.76	0.98	1.18	0.16	0.18	0.23	0.09	0.12
3.0	13	1.14	3.03	13.14	0.89	1.15	0.19	0.23	0.28	0.14	0.17
4.0	13	1.52	4.03	13.02	1.14	1.50	0.33	0.40	0.49	0.25	0.30
4.0	12	1.78	4.09	12.05	1.01	1.41	0.53	0.47	0.58	0.32	0.39
4.0	11	2.12	4.06	10.96	0.86	1.26	0.52	0.57	0.70	0.43	0.53
5.0	11	2.65	4.88	11.05	0.96	1.50	0.71	0.86	1.06	0.68	0.82
4.0	10	2.56	3.96	9.85	0.72	1.08	0.88	0.65	0.80	0.52	0.64
5.0	10	3.20	4.84	9.85	0.81	1.30	1.01	0.98	1.20	0.77	0.94
5.0	9	3.96	5.00	8.84	0.73	1.15	1.75	1.29	1.58	1.07	1.31

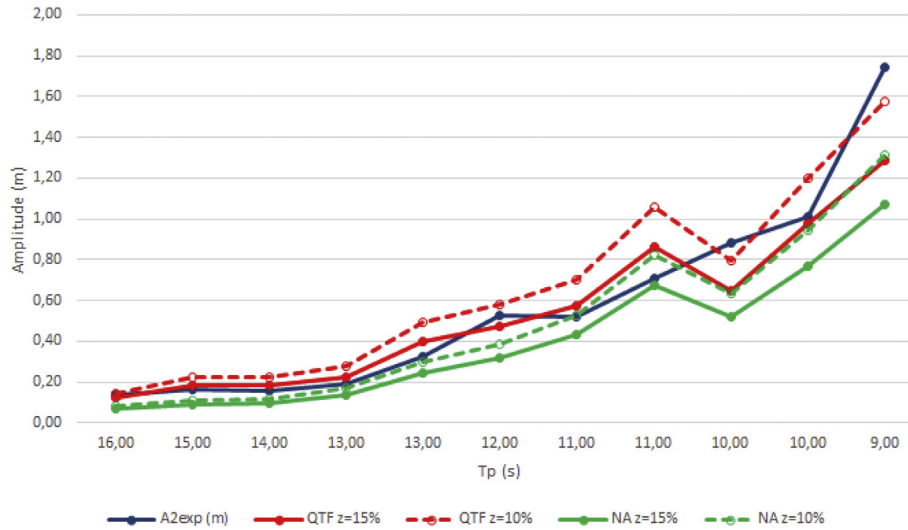


Fig. 27. Graphical representation of the mean slow-drift amplitudes obtained in tests with different peak periods (T_p). Values according to the results in Table 4. NA stands for Newman's approximation.

4.5.1. The use of the white-noise approximation

The use of Newman's approximation for estimating the slow-drift forces is a quite expedite procedure that allows for a significant reduction of the effort required to compute the difference-frequency forces. It is also widespread and consolidated in the analysis of deep-water moored systems with large resonant periods in the horizontal plane (typically above 100s). For the platform under analysis, however, the natural periods in surge and sway are relatively small, and the agreement between the results obtained with this approximation and those from the full QTFs is not as good, as shown in the previous section.

One may still envisage, however, the use of the white-noise approximation, since the main condition for this approach to be accurate is simply that the second-order motion spectrum should be narrow-banded. This condition is met due to the low damping levels observed in the drift motions, typically below 15% of the critical damping.

The present section brings an overview of the results obtained with the white-noise approach, when computing the second-order force spectrum according to Eq. (8). It should be reminded that the main advantage here is that the QTFs only need to be computed for pairs of frequencies with difference equal to the natural frequency of the drift motion. Consequently, the computational effort and time are largely reduced if compared to the computation of a full QTF matrix.

In order to illustrate the level of agreement in terms of the slow-drift motion spectrum, Fig. 28 presents a comparison of the second-order surge spectra computed with the different methods for the same test presented before in Fig. 25(a). Again, the results are obtained for two different damping levels, 10% (dashed lines) and 15% (solid lines) of the critical damping. One may realize that the motion-spectra obtained with the white-noise approach agree very well with the ones computed with the QTF matrix.

The overall agreement concerning the mean motion amplitudes obtained for the whole set of irregular wave tests may be inferred from the results in Table 5. The conditions are the same ones presented in Table 4, so part of the data is excluded in this case. The results show that the agreement remains very good for all wave periods and wave heights considered in the tests, the relative differences with the amplitudes obtained from the QTFs being always below 5%.

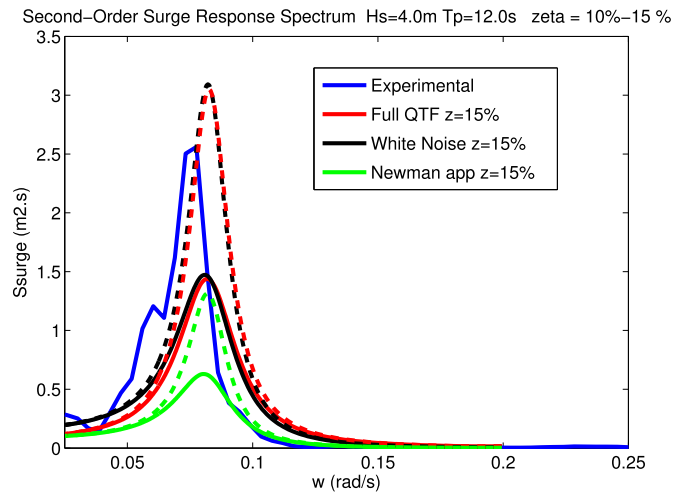


Fig. 28. Second-order Spectra for surge: $H_s = 4.0$ m, $T_p = 12$ s. Experimental spectrum (blue); from QTFs (red), from White Noise approximation (black) and from Newman's approximation (green) ($\zeta = 10\%$ dashed lines, $\zeta = 15\%$ solid lines). (For interpretation of the references to colour in this figure legend, the reader is referred to the web version of this article.)

Table 5

Mean second-order surge amplitudes (A_2) obtained for the different irregular wave tests: from experimental records (A_{2exp}); from numerical models considering the QTF and White Noise approximation (WN).

Hs (m)	Tp (s)	A2exp (m)	A2teo QTF (m)		A2teo WN (m)	
			z = 15%	z = 10%	z = 15%	z = 10%
2.50	16.00	0.14	0.12	0.14	0.11	0.14
3.00	15.00	0.17	0.19	0.23	0.18	0.22
3.00	14.00	0.16	0.18	0.23	0.19	0.23
3.00	13.00	0.19	0.23	0.28	0.23	0.29
4.00	13.00	0.33	0.40	0.49	0.41	0.51
4.00	12.00	0.53	0.47	0.58	0.48	0.59
4.00	11.00	0.52	0.57	0.70	0.58	0.71
5.00	11.00	0.71	0.86	1.06	0.87	1.07
4.00	10.00	0.88	0.65	0.80	0.66	0.81
5.00	10.00	1.01	0.98	1.20	1.00	1.22
5.00	9.00	1.75	1.29	1.58	1.30	1.59

Finally, the same results are presented in a graphical manner in Fig. 29, once again showing that the results obtained with the two different methods are almost indistinguishable.

Some additional comments regarding the use of the white-noise approach are necessary: First, one should remind that the white-noise approach still requires the computation of part of the QTF matrix. In the results shown above, the QTFs employed were those computed from WAMIT without considering any simplifications (the full second-order approach discussed in Sections 2 and 3). Nonetheless, it was shown in Section 3 that the QTFs obtained when the second-order potential was disregarded were also quite accurate. If employed as an alternative in the white-noise estimations, they would certainly lead to almost the same results. In this way, the gains obtained regarding the computational model would be even more remarkable, since not only fewer elements of the QTF matrix need to be computed, but also they can be computed without the need for modeling the free-surface.

Furthermore, the conditions for the white-noise approach seem to be less restrictive if compared to the ones for the Newman's approximation, since such approach does not involve, in principle, any restrictions concerning the water depth nor the natural frequencies of motion. The condition that the drift resonances occur under small damping levels seems to be met quite generally.

Finally, it must be said that the white noise approach adopted in the present work follows the procedure proposed in Ref. [34], which requires the use of the second-order force spectrum (Eq. (7)) and a decoupled transfer function of motion. However, Rezende et al. [43] have later proposed a somewhat different procedure when analyzing the resonant roll motions of an FLNG. In this case, instead of the force spectrum, the second-order force (QTF) was considered constant, and the authors also reported good results when following this approach. Although this procedure was not tested for the present results and the analysis in Ref. [43] concerned a very different floating system, this might be an additional alternative for simplifying the slow-drift computations.

5. Conclusions

A detailed investigation on the numerical estimations of the slow-drift forces of the HiPRWind platform was done. For this, an experimental campaign was conducted in two different facilities.

Both a horizontal elastic mooring and a catenary (chain) mooring were employed. The whole campaign comprised tests in regular, bichromatic and irregular waves. Wind effects have not been introduced in this phase of the research.

The numerical modeling has been carried out with the frequency domain solver WAMIT, and several options for evaluating the slow-drift forces were considered and tested against the experimental measurements. These options included approximations of the second-order diffraction forces, namely the one that disregards the effect of the second-order potential in the computations, the Newman's approximation, and the so-called white-noise approach. All of them lead to significant reductions of the effort and time required for performing the computations, but not all of them proved appropriate for the present design conditions. Moreover, since the confrontations between estimations and experimental measurements were mostly based on the drift motions, the results were evaluated considering a reasonable uncertainty in the damping levels.

In general, the results showed that:

1. First-order motions were accurately modeled considering the damping obtained from decay tests. Mean-drift forces in regular wave tests were also reasonably well predicted;
2. The slow-drift amplitudes predicted for different frequency pairs follow closely the trend observed in bichromatic wave tests. A reasonable agreement of the amplitudes was obtained for damping levels that were within the expected range, thus increasing the confidence on the numerical predictions. The same damping range was subsequently considered for the analysis of all the irregular wave tests;
3. Regarding the analysis of the slow-drift motions in irregular wave conditions, the predictions based on the full QTFs have shown a good agreement with the amplitudes observed in the model-tests;
4. The use of Newman's approximation led to an underestimation of the slow-drifts, indicating that this may not be the best option for the mooring design. It is supposed that the main reason for this lies in the relatively low natural periods of the horizontal excursions of the present design (around 75 s in surge), consequence of a somewhat stiff mooring system.

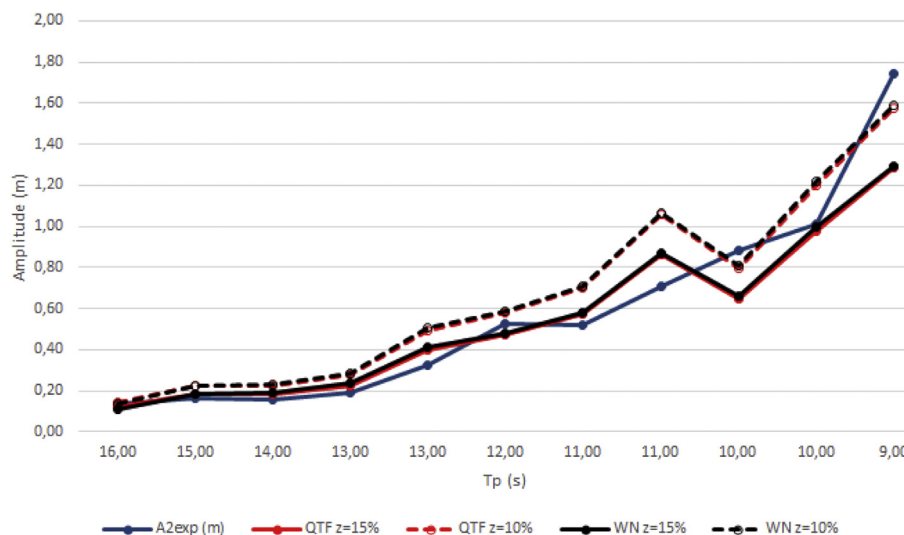


Fig. 29. Graphical representation of the mean slow-drift amplitudes obtained in tests with different peak periods (T_p). Values according to the results in Table 5. WN stands for the White-Noise approximation.

5. The white-noise approach was also tested, considering that the second-order force spectrum is constant when computing the motion spectra. In this analysis, the surge motion was decoupled from the other motions. Good results were achieved, with very small discrepancies compared to those obtained with the full QTF matrix. The use of this approach reduces the computational time substantially, requiring elements only in one diagonal of the QTF matrix;
6. The QTF values obtained when disregarding the second-order potential were very close to those obtained with the full second-order solution. Since the quadratic part of the QTF can be computed without the need to model the free-surface, this alternative may also lead to important savings in computational time. Furthermore, one should remember that guaranteeing the numerical convergence for the solution of the second-order problem is not a trivial task. In this case, therefore, not only time is saved, but also the robustness of the numerical model is ultimately improved.

In general, the results obtained in this campaign have shown that the slow-drifts observed in the model tests were well captured by the radiation-diffraction model for the whole range of peak periods tested, provided that a proper damping calibration was made. The selection of approximations for computing the QTFs must be done cautiously, observing especially the stiffness of the mooring system (natural periods) and the eventual effects of restricted water depths. Nonetheless, it was shown that with the use of an appropriate approximation, in particular the white noise one, the efforts involved in the numerical modeling and the computational time can be reduced substantially without a significant loss of accuracy.

It is important to highlight that, even though this methodology has been here systematically applied only in the context of a particular case study (a floater for a 1.5 Mw turbine), the analysis could be replicated for a more powerful one, in particular the 5–8 Mw designs that are under development at the moment. Indeed, the proposed improvements may have substantial impact on how slow-drift motions are treated in floating offshore wind turbine industry during design phase, leading to a change on the existing paradigm of either using Newman's or cumbersome full QTF computations to predict such motions.

The influence of wind effects has not been investigated up to this point. Besides increasing the mean drift, wind will probably be responsible for an increase of the drift damping, with an impact on the amplitude of the slow-drift motions. Benchmarking experimental tests including both wind and waves, as those expected for the OC5 program, will certainly be very important for verifying the behavior of the second-order dynamics in this more complex scenario.

Acknowledgments

The authors acknowledge the support from MARINET program, grant SEMISO: SEMI submersible Second Order, which provided funding for the tests conducted at ECN and particularly thank ECN Sylvain Bourdier for assistance in the raw data processing. Moreover, the use of the FP7 project HiPRWind geometry for the tests is gratefully accredited. Finally, authors are thankful to the data access provided by ACCIONA Energía, especially to Raul Manzananas, for the support on this investigation.

References

- [1] T. Hanson, B. Skaare, R. Yttervik, F. Nielsen, O. Havmøller, Comparison of Measured and Simulated Responses at the First Full Scale Floating Wind Turbine HYWIND, Tech. Rep., EWEA OFFSHORE, 2011.
- [2] D. Roddier, C. Cermelli, A. Aubault, A. Weinstein, WindFloat: a floating foundation for offshore wind turbines, *J. Renew. Sustain. Energy* 2 (3) (2010) 033104, <https://doi.org/10.1063/1.3435339>. <http://scitation.aip.org/content/aip/journal/jrse/2/3/10.1063/1.3435339>.
- [3] R. Nicholls-Lee, W. Micklethwaite, R. Walker, R. Argall, Novel, practical and effective: a feasibility study for a low motion, floating wind turbine platform, in: *ASME (Ed.), 33rd International Conference on Ocean, Offshore and Arctic Engineering (OMAE)*, 2014.
- [4] G. Marsh, Greater role for composites in wind energy, *Reinf. Plast.* 58 (1) (2014) 20–24, [https://doi.org/10.1016/S0034-3617\(14\)70037-2](https://doi.org/10.1016/S0034-3617(14)70037-2). <http://www.sciencedirect.com/science/article/pii/S0034361714700372>.
- [5] A.M. Viselli, A.J. Goupee, H.J. Dagher, Model test of a 1:8 scale floating wind turbine offshore in the Gulf of Maine, in: *ASME (Ed.), 33rd International Conference on Ocean, Offshore and Arctic Engineering (OMAE)*, 2014.
- [6] A.J. Coulling, A.J. Goupee, A.N. Robertson, J.M. Jonkman, H.J. Dagher, Validation of a FAST semi-submersible floating wind turbine numerical model with DeepCwind test data, *J. Renew. Sustain. Energy* 5 (2) (2013a) 023116, <https://doi.org/10.1063/1.4796197>. <http://scitation.aip.org/content/aip/journal/jrse/5/2/10.1063/1.4796197>.
- [7] D. Roddier, A. Peiffer, A. Aubault, J. Weinstein, A generic 5 MW WINDFLOAT for numerical tool validation & comparison against a generic spar, in: *ASME 30th International Conference on Ocean, Offshore and Arctic Engineering, OMAE2011*, 2011.
- [8] A.J. Goupee, B. Koo, R.W. Kimball, K.F. Lambrakos, H.J. Dagher, Experimental comparison of three floating wind turbine concepts, in: *ASME 31st International Conference on Ocean, Offshore and Arctic Engineering, OMAE2012*, 2012.
- [9] A.J. Goupee, B.J. Koo, R.W. Kimball, K.F. Lambrakos, H.J. Dagher, Experimental comparison of three floating wind turbine concepts, *J. Offshore Mech. Arct. Eng.* 136 (2) (2014) 020906, <https://doi.org/10.1115/1.4025804>.
- [10] H.R. Martin, R.W. Kimball, A.M. Viselli, A.J. Goupee, Methodology for Wind/wave basin testing of floating offshore wind turbines, in: *ASME 31st International Conference on Ocean, Offshore and Arctic Engineering, OMAE2012*, 2012.
- [11] B. Koo, A.J. Goupee, K.F. Lambrakos, R.W. Kimball, Model tests for a floating wind turbine on three different floaters, in: *ASME 31st International Conference on Ocean, Offshore and Arctic Engineering, OMAE2012*, 2012.
- [12] B.J. Koo, A.J. Goupee, R.W. Kimball, K.F. Lambrakos, Model tests for a floating wind turbine on three different floaters, *J. Offshore Mech. Arct. Eng.* 136 (2) (2014) 020907, <https://doi.org/10.1115/1.4024711>.
- [13] L. Roald, J. Jonkman, A. Robertson, N. Chokani, The effect of second-order hydrodynamics on floating offshore wind turbines, *Energy Procedia* 35 (0) (2013) 253–264, <https://doi.org/10.1016/j.egypro.2013.07.178>. <http://www.sciencedirect.com/science/article/pii/S1876610213012642>. deepWind 2013: selected papers from 10th Deep Sea Offshore Wind R&D Conference, Trondheim, Norway, 24, 25 January 2013.
- [14] A.J. Coulling, A.J. Goupee, A.M. Robertson, J.M. Jonkman, Importance of second-order difference-frequency wave-diffraction forces in the validation of a FAST semi-submersible floating wind turbine model, in: *ASME (Ed.), 32nd International Conference on Ocean, Offshore and Arctic Engineering (OMAE), OMAE2013*, 2013, p. 11072.
- [15] J.N. Newman, Second order, slowly varying forces on vessels in irregular Waves, in: *Int. Symp. Dynamics of Marine Vehicles and Struct. In Waves*, 1974, pp. 182–186.
- [16] S. Gueydon, T. Duarte, J. Jonkman, I. Bayati, A. Sarmento, Comparison of second order loads on a semisubmersible floating wind turbine, in: *ASME (Ed.), 33rd International Conference on Ocean, Offshore and Arctic Engineering (OMAE)*, 2014.
- [17] S. Gueydon, S. Weller, Study of a floating foundation for wind turbines, in: *ASME 31st International Conference on Ocean, Offshore and Arctic Engineering, OMAE2012*, 2012.
- [18] S. Gueydon, S. Weller, Study of a floating foundation for wind turbines, *J. Offshore Mech. Arct. Eng.* 135 (3) (2013) 031903, <https://doi.org/10.1115/1.4024271>.
- [19] A. Jiawen Li, B. Yougang Tang, C.R.W. Yeung, Effects of second-order difference-frequency wave forces on a new floating platform for an offshore wind turbine, *J. Renew. Sustain. Energy* 6 (3) (2014) 033102, <https://doi.org/10.1063/1.4872360>. <http://scitation.aip.org/content/aip/journal/jrse/6/3/10.1063/1.4872360>.
- [20] I. Bayati, J. Jonkman, A. Robertson, A. Platt, The effects of second-order hydrodynamics on a semisubmersible floating offshore wind turbine, *J. Phys. Conf. Ser.* 524 (1) (2014) 012094. <http://stacks.iop.org/1742-6596/524/i=1/a=012094>.
- [21] C. Lopez-Pavon, R.A. Watai, F. Ruggeri, A. Simos, A. Souto-Iglesias, Influence of wave induced second-order forces in semi-submersible FOWT mooring design, *J. Offshore Mech. Arct. Eng.* 137 (3) (2015) 031602–031612.
- [22] I. Bayati, S. Gueydon, M. Belloli, Study of the effect of water depth on potential flow solution of the OC4 semisubmersible floating offshore wind turbine, *Energy Procedia* 80 (2015) 168–176, <https://doi.org/10.1016/j.egypro.2015.11.419>. <http://www.sciencedirect.com/science/article/pii/S1876610215021517>, 12th Deep Sea Offshore Wind R&D Conference, EERA DeepWind'2015.
- [23] S. Lefebvre, M. Collu, Preliminary design of a floating support structure for a 5MW offshore wind turbine, *Ocean. Eng.* 40 (0) (2012) 15–26, <https://doi.org/>

[1] T. Hanson, B. Skaare, R. Yttervik, F. Nielsen, O. Havmøller, Comparison of Measured and Simulated Responses at the First Full Scale Floating Wind

- 10.1016/j.oceaneng.2011.12.009. <http://www.sciencedirect.com/science/article/pii/S0029801811002769>.
- [24] M. Brommundt, L. Krause, K. Merz, M. Muskulus, Mooring system optimization for floating wind turbines using frequency domain analysis, *Energy Procedia* 24 (0) (2012) 289–296, <https://doi.org/10.1016/j.egypro.2012.06.111>. <http://www.sciencedirect.com/science/article/pii/S1876610212011514>.
- [25] M.I. Kvittem, E.E. Bachynski, T. Moan, Effects of hydrodynamic modelling in fully coupled simulations of a semi-submersible wind turbine, *Energy Procedia* 24 (0) (2012) 351–362, <https://doi.org/10.1016/j.egypro.2012.06.118>. <http://www.sciencedirect.com/science/article/pii/S1876610212011587>. selected papers from Deep Sea Offshore Wind R&D Conference, Trondheim, Norway, 19–20 January 2012.
- [26] J.E. Gutierrez-Romero, B. Zamora, J. Garcia-Espinosa, M.R. Peyrau, Tool development based on FAST for performing design optimization of offshore wind turbines: FASTLognoter, *Renew. Energy* 55 (0) (2013) 69–78, <https://doi.org/10.1016/j.renene.2012.12.026>. <http://www.sciencedirect.com/science/article/pii/S0960148112007926>.
- [27] J.E. Gutierrez-Romero, J. Garcia-Espinosa, B. Servan-Camas, B. Zamora-Parra, Non-linear dynamic analysis of the response of moored floating structures, *Mar. Struct.* 49 (2016) 116–137, <https://doi.org/10.1016/j.marstruc.2016.05.002>. <http://www.sciencedirect.com/science/article/pii/S0951833916300636>.
- [28] H. Kim, J. Choung, G.Y. Jeon, Design of mooring lines of floating offshore wind turbine in Jeju offshore area, in: *Asme (Ed.), 33rd International Conference on Ocean, Offshore and Arctic Engineering (OMAE)*, 2014.
- [29] L. Castro-Santos, V. Diaz-Casas, Life-cycle cost analysis of floating offshore wind farms, *Renew. Energy* 66 (0) (2014) 41–48, <https://doi.org/10.1016/j.renene.2013.12.002>. <http://www.sciencedirect.com/science/article/pii/S0960148113006642>.
- [30] M. Kim, K. Yue, The second-order diffraction solution for an axisymmetric body - part 1. monochromatic waves, *J. Fluid Mech.* 200 (1989) 235–264.
- [31] M. Kim, K. Yue, The complete second-order diffraction solution for an axisymmetric body - part 2. bichromatic waves and body motions, *J. Fluid Mech.* 211 (1990) 547–593.
- [32] J. Pinkster, *Low Frequency Second Order Wave Exciting Forces on Floating Structures*, Publication (Nederlands Scheepsbouwkundig Proefstation); Netherlands Ship Model Basin, 1980. <http://books.google.es/books?id=lvXYGwAACAAJ>.
- [33] J. Aranha, A. Fernandes, On the second-order slow drift force spectrum, *Appl. Ocean Res.* 17 (5) (1995) 311–313, [https://doi.org/10.1016/0141-1187\(95\)00013-5](https://doi.org/10.1016/0141-1187(95)00013-5). <http://www.sciencedirect.com/science/article/pii/S0141118795000135>.
- [34] V. Matos, A. Simos, S. Sphaier, Second-order resonant heave, roll and pitch motions of a deep-draft semi-submersible: theoretical and experimental results, *Ocean. Eng.* 38 (17–18) (2011) 2227–2243, <https://doi.org/10.1016/j.oceaneng.2011.10.005>. <http://www.sciencedirect.com/science/article/pii/S0029801811002368>.
- [35] S. Crandall, W. Mark, *Random Vibration in Mechanical Systems*, Academic Press, New York, 1963.
- [36] H. Wadhwa, K.P. Thiagarajan, Experimental assessment of hydrodynamic coefficients of disks oscillating near a free surface, in: *ASME 28th International Conference on Offshore Mechanics and Arctic Engineering, OMAE*, 2009.
- [37] C. Lopez-Pavon, A. Souto-Iglesias, Hydrodynamic coefficients and pressure loads on heave plates for semi-submersible floating offshore wind turbines: a comparative analysis using large scale models, *Renew. Energy* 81 (0) (2015) 864–881, <https://doi.org/10.1016/j.renene.2015.04.003>. <http://www.sciencedirect.com/science/article/pii/S0960148115002839>.
- [38] B. Reguero, M. Menéndez, F. Méndez, R. Mínguez, I. Losada, A global ocean wave (GOW) calibrated reanalysis from 1948 onwards, *Coast. Eng.* 65 (2012) 38–55.
- [39] WAMIT, WAMIT 6.4/6.4S User Manual. The Massachusetts Institute of Technology, 2014.
- [40] P.R. de Reilhac, F. Bonnefoy, J. Rousset, P. Ferrant, Improved transient water wave technique for the experimental estimation of ship responses, *J. Fluids Struct.* 27 (3) (2011) 456–466, <https://doi.org/10.1016/j.jfluidstruct.2011.01.002>. <http://www.sciencedirect.com/science/article/pii/S0889974611000053>.
- [41] M. Soylemez, M. Atlar, A comparative study of two practical methods for estimating the hydrodynamic loads and motions of a semi-submersible, *J. Offshore Mech. Arct. Eng.* 122 (1) (1999) 57–63.
- [42] S.G. Tan, W.C. De-Boom, The wave-induced motion of a tension leg platform in deep water, Paper OTC 4074, in: *Offshore Technology Conference, OTC*, 1981, pp. 89–98.
- [43] F.C. Rezende, A.C. de Oliveira, X. Chen, F. Menezes, A comparison of different approximations for computation of second order roll motions for a flng, in: *ASME 32nd International Conference on Ocean, Offshore and Arctic Engineering, OMAE2013*, 2013.